Nodally integrated thermomechanical RKPM: Part I — Thermoelasticity

Michael Hillman*† and Kuan-Chung Lin‡

Note: This is a pre-print of an article under review.

Abstract

In this two-part paper, a stable and efficient nodally-integrated reproducing kernel particle method (RKPM) is introduced for solving the governing equations of generalized thermomechanical theories. Part I investigates quadrature in the weak form using coupled and uncoupled classical thermoelasticity as model problems. It is first shown that nodal integration of these equations results in spurious oscillations in the solution many orders of magnitude greater than pure elasticity. A naturally stabilized nodal integration is then proposed for the coupled equations. The variational consistency conditions for nth order exactness and convergence in the two-field problem are then derived, and a uniform correction on the test function approximations is proposed to achieve these conditions. Several benchmark problems are solved to demonstrate the effectiveness of the proposed method. In the sequel, these methods are developed for generalized thermoelasticity and generalized finite-strain thermoplasticity theories of the hyperbolic type that are amenable to efficient explicit time integration.

keywords Meshfree, thermoelasticity, nodal integration, naturally stabilized nodal integration, variationally consistent integration, coupled problems

1 Introduction

The interaction between temperature, stress, and deformation is an important consideration in many engineering problems. The need for solving these partially- or fully-coupled systems may arise due to the presence of fracture, bending, contact, and friction, among other phenomena. Certain sub-classes of these problems such as additive and subtractive manufacturing also involve a large degree of material deformation, flow, and failure, with associated topological changes in the domain. Here, the use of mesh-based methods for analysis is obviously non-trivial. On the other hand, meshfree methods are adept at handling these phenomena, yet an effective solution technique requires careful treatment of quadrature, which is essentially an open-problem for meshfree thermomechanical analysis. In addition, the time step restriction for the associated classical parabolic type of energy equation is too restrictive for explicit analysis, which is often used for meshfree methods in extreme-deformation problems. The subject of this two-part paper is to address these issues and propose a stable and efficient meshfree technique for thermomechanical problems under the reproducing kernel particle method (RKPM) framework [39, 12, 40], which possesses nth-order accuracy and associated optimal convergence rates in smooth problems [40].

*Kimball Assistant Professor, Department of Civil and Environmental Engineering, The Pennsylvania State University, University Park, PA 16802, USA.

†Corresponding author; email: mhillman@psu.edu; postal address: 224A Sackett Building, The Pennsylvania State University, University Park, PA 16802, USA.

‡Assistant Professor, Department of Civil Engineering, National Cheng Kung University, Tainan 70101, Taiwan, ROC.

In this first part, efficient and stable quadrature of the Galerkin weak form for thermomechanical analysis is developed using classical thermoelasticity as a model problem. In the sequel, these approaches are extended to generalized thermoelasticity and generalized finite-strain plasticity theories of the hyperbolic type.

Due to the limitations of closed-form solutions to the classical thermoelastic equations e.g., [18, 19, 56, 5], numerical techniques are of course desired for more complex geometries and boundary conditions, in other words, applications. Numerical approaches to the classical theory have been developed over the past several decades, including finite element-based approaches [33, 6, 7, 48, 32] and boundary element methods [55, 8, 57, 29].

Meshfree methods [10] have also been developed for both coupled and uncoupled thermoelasticity. The element-free Galerkin method (EFG) has been used to solve the problem of shape optimization in linear thermoelastic solids [4]. The meshless local Petrov-Galerkin method (MLPG) has been employed for problems with orthotropic material properties [54], using various trial approximations [17, 50, 67]. Later, direct MLPG [23] was developed for thermoelasticity.

In these approaches, EFG uses quadrature points based on background cells which necessitates very high order (and thus expensive) quadrature for acceptable accuracy [20, 14, 11, 66]. For MLPG, integration is performed over local meshfree nodal domains, employing several quadrature points per cell, which is also expensive [24]. In addition, as recently shown in [66], even high-order quadrature is not variationally consistent (VC) [11], and it is theoretically impossible to converge at optimal rates and achieve the level of accuracy offered by the trial functions employed in the Galerkin solution with traditional quadrature. In [66], this analytical result was unequivocally demonstrated, offering new insight into the importance of alternative integration approaches in meshfree methods.

In contrast to classical approaches, nodal integration methods generally employ one quadrature point per node, and can greatly accelerate meshfree computations. They are also favored due to their relative simplicity, and their ability to preserve the mesh-free characteristics of the method on the quadrature level. Yet pure nodal integration, known as direct nodal integration (DNI) in the literature, exhibits poor solution accuracy and spatial instability in the form of oscillations [24]. The instability arises due to a zero gradient at nodal points for modes with a wavelength of twice the nodal spacing [2, 3, 14], severely under-sampling the strain energy density. Thus small-wavelength modes are admitted in the solution with little to no resistance, and can hence either severally pollute the solution or grow unbounded.

To circumvent this issue, several stabilized nodal integration methods have been proposed. In [2] a residual-based method was developed that supplements the Galerkin formulation with second-order gradient terms, which are non-zero at nodes. This method however necessitates the computation of high-order meshfree gradients which are expensive, and it is not clear how to straightforwardly generalize a residual approach to non-linear solid mechanics. Stress points [51, 22] can eliminate the instability by sampling the internal energy at locations away from the nodes, but this can significantly increase the computational cost. A highly efficient stabilized conforming nodal integration (SCNI) has been proposed [14], which stabilizes the solution by employing strain-smoothing, and further provides first-order variational consistency (Galerkin exactness). A modified SCNI (MSCNI) has been developed [9, 49] to alleviate some remaining instabilities in SCNI when the discretization is sufficiently fine or the surface to volume ratio is small. Additional integration points are added in the nodal subdomain to sample the solution away from the nodes, similar to stress points. Taylor series expansions on strains [45, 38, 24, 44] (which originates from the finite element method [41]) and related methods [64, 63] can also stabilize the solution, and avoid the expense of sampling/stress points. In order to reduce the computational cost of meshfree gradients of strain in this method, a naturally stabilized nodal integration (NSNI) has been proposed [24] which employs implicit gradients (originating from synchronized derivatives [35] and the reproducing kernel hierarchical partition of unity method [36, 37]). This approach has been shown to accelerate computations by an order of magnitude over sampling point-type methods [24].

In order to correct the accuracy of nodal integration methods, several additional/combined approaches have been developed. In [14] it was shown that a condition exists on the numerical inte-

gration and test function in order to obtain first-order Galerkin exactness. This can be achieved using the SCNI technique via conforming strain smoothing. Later, the condition was generalized to the concept of variational consistency [11], or the conditions for arbitrary nth order exactness, where a correction was proposed to uniformly correct any choice of quadrature including nodal integration. The corrected integration methods using this approach are herein given a prefix as "VC-", e.g., VC-NSNI. SCNI has been extended under various frameworks to achieve higher-order variational consistency, such as quadratically consistent integration [21], and reproducing kernel gradient smoothing [60].

So far, only the strain-gradient methods in [64, 63] have been applied to thermomechanical analysis [65]. Staggered time integration was employed to overcome the time step restriction in the energy equation, and momentum smoothing was used for stabilization, both of which complicate the overall solution algorithm. In addition, the nodal integration employed violates the critical condition of variational consistency. The only other related methods are for the tangential problem of porous media. In [62], MSCNI was developed for poromechanics. To avoid the limitation of conforming cells in extreme deformation problems, a non-conforming version was proposed in [53, 42], but the relaxation of the conforming condition in strain-smoothing results in a loss of variational consistency and thus convergence [11]. To greatly reduce the computational cost of MSCNI, and circumvent the limitations of non-conforming methods, VC-NSNI was recently proposed for porous media simulation [61]. There the VC conditions for first order exactness were derived, yet an approximate lower-order condition was instead corrected for.

In this work, a nodally-integrated RKPM is developed for thermomechanical analysis. In Part I of this series, the VC conditions for arbitrary-order accuracy in the Galerkin solution of the coupled problem of thermoelasticity are derived. It is shown that the conditions here require additional restrictions on the test functions compared to pure elasticity. A variationally consistent correction is then proposed to exactly satisfy the constraints up to nth order. To stabilize the meshfree solution, a naturally stabilized nodal integration is further proposed. Here it is shown that for thermoelastic problems, the solution instability in DNI results in oscillations *many orders of magnitude greater than in pure elasticity*, yielding meaningless results. The combined method VC-NSNI is then applied to several quasi-static and dynamic thermoelastic benchmark problems where stability and high accuracy in RKPM are achieved using the proposed nodal integration. Part II of this work extends these methods to generalized thermoelasticity theories and generalized finite-strain thermoplasticity, both of the hyperbolic type, in order to facilitate accelerated computations in explicit dynamics and a uniform time integration on displacement and temperature variables.

The remainder of this paper is organized as follows. The equations of thermoelasticity are given in Section 2. In Section 3 the reproducing kernel approximation is reviewed. Section 4 explores the challenges and instabilities in direct nodal integration for thermoelasticity. In Sections 5-7 NSNI, variationally consistent integration (VCI), and VC-NSNI are introduced for thermoelasticity. Numerical implementation details are given in Section 8, with the matrix forms and Newmark algorithm for the thermoelastic equations. Several static, quasi-static, and dynamic benchmarks problems are solved in Section 9, with the proposed thermomechanical RKPM results compared with analytical solutions, and solutions by other numerical methods. Concluding remarks are then given in Section 10.

2 Governing equations and weak formulation

2.1 Strong form of thermoelasticity

2.1.1 Equations of motion and energy conservation

Consider a domain Ω $]0, t_f[$ with boundary $\partial\Omega$ $]0, t_f[$. The governing equations for linear thermoelasticity on the domain are [47]:

$$r \quad \boldsymbol{\sigma} + \boldsymbol{b} = \rho \ddot{\boldsymbol{u}} \tag{1}$$

$$r \quad q \quad \rho c_p \dot{\theta} + Q \quad \beta T_0 \, r \quad \dot{u} = 0 \tag{2}$$

where r is the Del operator, $\boldsymbol{\sigma}$ is the Cauchy stress tensor, $\boldsymbol{b}$ is a prescribed body force, ρ is the density, $\ddot{\boldsymbol{u}}$ $\partial^2 \boldsymbol{u}/\partial t^2$ is the acceleration; $\boldsymbol{u}$ is the displacement field and herein is treated as a primary unknown, $\boldsymbol{q}$ is the heat flux, c_p is the heat capacity, θ T T_0 is the temperature difference and is treated as a primary unknown; T is the absolute temperature, T_0 is the reference temperature and $\dot{\theta}$ $\partial\theta/\partial t$; Q is a prescribed heat source, $\beta = \bar{\alpha}(3\lambda + 2\mu)$ is the thermal stress modulus; $\bar{\alpha}$ is the thermal expansion coefficient, λ and μ are Lamé's first and second constants; and $\dot{\boldsymbol{u}}$ $\partial \boldsymbol{u}/\partial t$ is the velocity.

Equation (1) is the conservation of linear momentum and (2) is the energy equation, or first law of thermodynamics (under specific assumptions). The nature of coupling between the two primary fields of displacement $\boldsymbol{u}$ and temperature difference θ is dictated by the prescribed constitutive laws for $\boldsymbol{\sigma}$ and $\boldsymbol{q}$.

Note that for the linear thermoelasticity, a small increment of the temperature difference compared with the reference temperature is assumed [47], that is

$$\frac{j\theta j}{T_0} \quad 1. \tag{3}$$

The boundary conditions associated with (1) and (2) are

$$\boldsymbol{u} = \boldsymbol{g} \quad \text{on } \partial\Omega_g \quad]0, t_f[\tag{4a}$$
$$\boldsymbol{\sigma} \quad \boldsymbol{n} = \boldsymbol{h} \quad \text{on } \partial\Omega_h \quad]0, t_f[\tag{4b}$$
$$\theta = \bar{\theta} \quad \text{on } \partial\Omega_T \quad]0, t_f[\tag{4c}$$
$$\boldsymbol{q} \quad \boldsymbol{n} = \bar{q} \quad \text{on } \partial\Omega_q \quad]0, t_f[\tag{4d}$$

where $\boldsymbol{g}$, $\boldsymbol{n}$, $\boldsymbol{h}$, $\bar{\theta}$, and $\bar{q}$ denote the prescribed displacement, outward unit normal to the boundary, prescribed traction, prescribed temperature difference, and prescribed heat flux, respectively, with $\overline{\partial\Omega_g \; [\; \partial\Omega_h} = \overline{\partial\Omega_T \; [\; \partial\Omega_q} = \partial\Omega$ and $\partial\Omega_g \; \backslash \; \partial\Omega_h = \partial\Omega_T \; \backslash \; \partial\Omega_q = ?$.

The complete problem in time is specified with the initial conditions at time $t = 0$ for $\boldsymbol{u}(\boldsymbol{x}, t)$ and $\theta(\boldsymbol{x}, t)$. Here we consider:

$$\boldsymbol{u}(\boldsymbol{x}, 0) = \boldsymbol{u}_0(\boldsymbol{x}), \quad \dot{\boldsymbol{u}}(\boldsymbol{x}, 0) = \boldsymbol{v}_0(\boldsymbol{x}), \quad \theta(\boldsymbol{x}, 0) = \theta_0(\boldsymbol{x}). \tag{5}$$

To complete the problem in space, the constitutive laws need to be prescribed. Without loss of generality, we consider a homogeneous isotropic media.

Classical isotropic thermoelasticity considers the Duhamel-Neumann law, which yields the relation between stress, strain, and temperature change. Herein, we consider the law with no prestrain:

$$\boldsymbol{\sigma} = \mathsf{C} : \boldsymbol{\varepsilon}(\boldsymbol{u}) \quad \beta\theta \mathsf{I} \tag{6}$$

where $\boldsymbol{\varepsilon}(\boldsymbol{u})$ $\frac{1}{2}(r \, \boldsymbol{u} + (r \, \boldsymbol{u})^{\mathsf{I}})$ is the strain tensor, C denotes the isotropic forth-order elasticity tensor, and I denotes the second-order identity tensor.

For the heat flux, the classical Fourier law is employed with isotropic heat conduction:

$$\boldsymbol{q} = \quad k \, r \, \theta \tag{7}$$

where k is the thermal conductivity. The reason for the specificity of these definitions will be clear in the sequel, where alternative relations are employed.

Employing (6) and (7), the governing equations (1) and (2) can be expressed directly in terms of the displacement $\boldsymbol{u}$ and temperature change θ:

$$r \quad (\mathsf{C} : \boldsymbol{\varepsilon}(\boldsymbol{u}) \quad \beta\theta \mathsf{I}) + \boldsymbol{b} = \rho \ddot{\boldsymbol{u}}, \tag{8a}$$
$$r \quad k \, r \, \theta \quad \rho c_p \dot{\theta} + Q \quad \beta T_0 \, r \quad \dot{\boldsymbol{u}} = 0. \tag{8b}$$

2.2 Coupling parameter and dimensionless variables

2.2.1 Coupling parameter

To distinguish between a fully coupled and a partially coupled (also called uncoupled) problem, the following thermoelastic parameter is introduced for convenience:

$$\delta = \frac{\beta^2 T_0}{\rho c_p(\lambda + 2\mu)}. \tag{9}$$

When $\delta = 0$ the system is uncoupled. On the other hand, if δ is a non-zero value, it is the fully coupled case. Here the case where a fully coupled thermomechanical analysis should be considered is clear: only when the material constants yield δ 0, an uncoupled system can be used. This is often the case with metals.

In this paper, the coupled and uncoupled thermoelastic equations are studied; we use $\delta = 1$ and $\delta = 0$, respectively, with all parameters given except T_0, which is calculated using (9):

$$T_0 = \frac{\delta \rho c_p(\lambda + 2\mu)}{\beta^2}. \tag{10}$$

2.2.2 Dimensionless variables

The solutions in this manuscript are interpreted in terms of the following dimensionless variables:

$$\bar{y} = \frac{y}{a}, \quad \bar{\theta} = \frac{\theta}{T_0}, \quad \bar{t} = \frac{\kappa}{a^2}t, \quad \bar{\sigma} = \frac{\sigma}{\beta T_0}, \quad \bar{u} = \frac{(\lambda + 2\mu)}{a\beta T_0}u, \tag{11}$$

where $a = \kappa/(c_s \rho c_p)$; $\kappa = k/(\rho c_p)$, and $c_s = \sqrt{(\lambda + 2\mu)/\rho}$.

2.3 Weak form of thermoelasticity

Galerkin meshfree methods such as RKPM employ weak forms of the governing equations (8). Starting from the weighted residual approach, applying integration-by-parts and the divergence theorem these can be derived as: find $\boldsymbol{u}\ 2\ U_g$, and $\theta\ 2\ \Theta_T$, such that for all $\boldsymbol{v}\ 2\ U_0$, and $S\ 2\ \Theta_0$, the following equations hold:

$$\int \rho \boldsymbol{v} \quad \ddot{\boldsymbol{u}} d\Omega + \int \boldsymbol{\varepsilon}(\boldsymbol{v}) : \mathsf{C} : \boldsymbol{\varepsilon}(\boldsymbol{u}) d\Omega \quad \int \beta \, r \quad \boldsymbol{v} \theta d\Omega = \int \boldsymbol{v} \quad \boldsymbol{b} d\Omega + \int_{\partial \quad h} \boldsymbol{v} \quad \boldsymbol{h} d\Gamma, \tag{12a}$$

$$\int k \, r \, S \quad r \, \theta d\Omega + \int \rho c_p S \dot{\theta} d\Omega \quad \int \beta T_0 S \, r \quad \dot{\boldsymbol{u}} d\Omega = \int S Q d\Omega + \int_{\partial \quad q} S \bar{q} d\Gamma, \tag{12b}$$

with

$$U_g = f \boldsymbol{u} \ j \ \boldsymbol{u}\ 2\ H^1, \boldsymbol{u} = \boldsymbol{g} \text{ on } \partial\Omega_g \quad]0, t_f[g, \tag{13a}$$

$$U_0 = f \boldsymbol{v} \ j \ \boldsymbol{v}\ 2\ H^1, \boldsymbol{v} = \boldsymbol{0} \text{ on } \partial\Omega_g \quad]0, t_f[g, \tag{13b}$$

$$\Theta_T = f \theta \ j \ \theta\ 2\ H^1, \theta = \bar{\theta} \quad \text{on } \partial\Omega_T \quad]0, t_f[g, \tag{13c}$$

$$\Theta_0 = f S \ j \ S\ 2\ H^1, S = 0 \text{ on } \partial\Omega_T \quad]0, t_f[g. \tag{13d}$$

In (12), both bilinear "stiffness" integrals contain gradients of the primary unknown, $r\,\boldsymbol{u}$ and $r\,\theta$, in (12a) and (12b), respectively. Thus, when discretized by meshfree shape functions, it is easy to show that an oscillatory mode in both the displacement and temperature with a wavelength of twice the nodal spacing will not contribute to these terms away from the boundary, and this mode can potentially grow unrestricted [27].

Note that meshfree approximations generally do not meet the requirements (13) and need special techniques to impose essential boundary conditions. Here we employ the transformation method [13] with consistent weak forms [28] to attain Galerkin exactness in VC methods. The details are omitted for clarity of presentation of the proposed formulation; for details see [13, 28].

2.4 Galerkin form of thermoelasticity

The Galerkin statement of the problem (12) is: find $\boldsymbol{u}^h \ 2 \ U_g^h$, and $\theta^h \ 2 \ \Theta_T^h$, such that for all $\boldsymbol{v}^h \ 2 \ U_0^h$, and $S^h \ 2 \ \Theta_0^h$, the following equations hold:

$$\int \rho \boldsymbol{v}^h \quad \ddot{\boldsymbol{u}}^h d\Omega + \int \boldsymbol{\varepsilon}(\boldsymbol{v}^h) : \mathsf{C} : \boldsymbol{\varepsilon}(\boldsymbol{u}^h) d\Omega \quad \int \beta \, r \quad \boldsymbol{v}^h \theta^h d\Omega = \int \boldsymbol{v}^h \quad \boldsymbol{b} d\Omega + \int_{\partial \quad _h} \boldsymbol{v}^h \quad \boldsymbol{h} d\Gamma, \quad (14a)$$

$$\int k \, r \, S^h \quad r \, \theta^h d\Omega + \int \rho c_p S^h \dot{\theta^h} d\Omega \quad \int \beta T_0 S^h \, r \quad \dot{\boldsymbol{u}^h} d\Omega = \int SQ d\Omega + \int_{\partial \quad _q} S^h \bar{q} d\Gamma, \quad (14b)$$

with $U_g^h \quad U_g$, $\Theta_T^h \quad \Theta_T$, $U_0^h \quad U_0$, and $\Theta_0^h \quad \Theta_0$. The above necessitates quadrature, which motivates the current work. Gaussian integration sufficient for acceptable accuracy is prohibitively expensive, whereas nodal integration is extremely unstable, as will be seen.

3 Meshfree approximation

In this section, the reproducing kernel approximation is briefly reviewed. An overview of the implicit gradient is further given, which significantly lowers the computational cost of computing gradient terms in the stabilized formulation.

3.1 Reproducing Kernel approximation

Let a domain $\bar{\Omega} = \Omega \ [\ \partial\Omega$ be discretized by a set of NP nodes $\mathsf{S} = \mathsf{f}\mathbf{x}_I \mathsf{j}\mathbf{x}_I \ 2 \ \bar{\Omega}\mathsf{g}_{I=1}^{NP}$ with set of node numbers $\mathsf{N} = \mathsf{f}I\mathsf{j}\mathbf{x}_I \ 2 \ \mathsf{Sg}$. The nth order reproducing kernel (RK) approximation $u^h(\boldsymbol{x})$ of a function $u(\boldsymbol{x})$ is [39, 12, 40]:

$$u^h(\boldsymbol{x}) = \sum_{I 2 N} \Psi_I(\boldsymbol{x}) u_I \quad (15)$$

where $\mathsf{f}\Psi_I(\boldsymbol{x})\mathsf{g}_{I 2 N}$ is the set of RK shape functions, and $\mathsf{f}u_I\mathsf{g}_{I 2 N}$ are the associated coefficients. Note that the summation in (15) is only carried out over non-zero shape functions local to $\boldsymbol{x}$ in practice, naturally defining connectivity.

The shape functions in (15) are constructed by the product of a kernel function $\Phi_a(\boldsymbol{x} \quad \boldsymbol{x}_I)$ with normalized support a and a correction function $C(\boldsymbol{x}; \boldsymbol{x} \quad \boldsymbol{x}_I)$:

$$\Psi_I(\boldsymbol{x}) = \Phi_a(\boldsymbol{x} \quad \boldsymbol{x}_I) C(\boldsymbol{x}; \boldsymbol{x} \quad \boldsymbol{x}_I). \quad (16)$$

The correction function here is composed of a linear combination of nth order complete monomials, which allows the exact reproduction of these monomials. In matrix form the correction can be expressed as:

$$C(\boldsymbol{x}; \boldsymbol{x} \quad \boldsymbol{x}_I) = \boldsymbol{H}(\boldsymbol{x} \quad \boldsymbol{x}_I)^{\mathsf{I}} \boldsymbol{b}(\boldsymbol{x}). \quad (17)$$

where $\boldsymbol{H}(\boldsymbol{x} \quad \boldsymbol{x}_I)$ is a column vector of the monomials:

$$\boldsymbol{H}(\boldsymbol{x} \quad \boldsymbol{x}_I) = \left[1, x_1 \quad x_{1I}, x_2 \quad x_{2I}, x_3 \quad x_{3I}, (x_1 \quad x_{1I})^2, \quad , (x_3 \quad x_{3I})^n\right]^{\mathsf{I}} \quad (18)$$

and $\boldsymbol{b}(\boldsymbol{x})$ is a column vector of coefficients to be determined from the following nth order discrete reproducing conditions:

$$\sum_{I 2 N} \Psi_I(\boldsymbol{x}) \boldsymbol{H}(\boldsymbol{x}_I) = \boldsymbol{H}(\boldsymbol{x}) \quad \text{or} \quad \sum_{I 2 N} \Psi_I(\boldsymbol{x}) \boldsymbol{H}(\boldsymbol{x} \quad \boldsymbol{x}_I) = \boldsymbol{H}(\boldsymbol{0}) \quad (19)$$

which leads to $\boldsymbol{b}(\boldsymbol{x})$ of the following form:

$$\boldsymbol{b}(\boldsymbol{x}) = \boldsymbol{M}(\boldsymbol{x}) \ ^1 \boldsymbol{H}(\boldsymbol{0}) \quad (20)$$

where the moment matrix $\boldsymbol{M}$ is defended as follows:

$$\boldsymbol{M}(\boldsymbol{x}) = \sum_{I2N} \boldsymbol{H}(\boldsymbol{x} \quad \boldsymbol{x}_I)\boldsymbol{H}(\boldsymbol{x} \quad \boldsymbol{x}_I)^{\mathsf{I}} \Phi_a(\boldsymbol{x} \quad \boldsymbol{x}_I). \tag{21}$$

Employing (20), the RK shape functions are constructed as:

$$\Psi_I(\boldsymbol{x}) = \boldsymbol{H}(\boldsymbol{0})^{\mathsf{I}} \boldsymbol{M}(\boldsymbol{x}) \quad ^1\boldsymbol{H}(\boldsymbol{x} \quad \boldsymbol{x}_I)\Phi_a(\boldsymbol{x} \quad \boldsymbol{x}_I). \tag{22}$$

The shape function gradient necessary in the weak form can be computed straightforwardly based on the product rule:

$$\begin{aligned} r\,\Psi_I(\boldsymbol{x}) = \boldsymbol{H}(\boldsymbol{0})^{\mathsf{I}}\, r\,(\boldsymbol{M}(\boldsymbol{x}) \quad ^1)\boldsymbol{H}(\boldsymbol{x} \quad \boldsymbol{x}_I)\Phi_a(\boldsymbol{x} \quad \boldsymbol{x}_I) \\ + \boldsymbol{H}(\boldsymbol{0})^{\mathsf{I}} \boldsymbol{M}(\boldsymbol{x}) \quad ^1\, r\, \boldsymbol{H}(\boldsymbol{x} \quad \boldsymbol{x}_I)\Phi_a(\boldsymbol{x} \quad \boldsymbol{x}_I) \\ + \boldsymbol{H}(\boldsymbol{0})\boldsymbol{M}(\boldsymbol{x}) \quad ^1\boldsymbol{H}(\boldsymbol{x} \quad \boldsymbol{x}_I)\, r\, \Phi_a(\boldsymbol{x} \quad \boldsymbol{x}_I) \end{aligned} \tag{23}$$

where

$$r\,(\boldsymbol{M}(\boldsymbol{x}) \quad ^1) = \quad \boldsymbol{M}(\boldsymbol{x}) \quad ^1\, r\, \boldsymbol{M}(\boldsymbol{x})\boldsymbol{M}(\boldsymbol{x}) \quad ^1. \tag{24}$$

However, the computational cost of computing this gradient is non-trivial (cf. [30]). Therefore a so-called *implicit* gradient (which originated from the synchronized derivative [35]) has been developed [16, 43] to save computational cost. This approximation preserves the essential properties of the explicit gradient, that is, the gradient reproducing properties of (23) (see (19) for reference)

$$\sum_{I=1}^{NP} r\,\Psi_I(\boldsymbol{x})\boldsymbol{H}(\boldsymbol{x}_I) = r\,\boldsymbol{H}(\boldsymbol{x}) \tag{25}$$

are satisfied by the implicit gradient reproducing kernel shape function.

Starting from the analogy of (16), the implicit gradient shape function is constructed as [16, 35]

$$\Psi^{\mathsf{O}}_{Ii}(\boldsymbol{x}) = \Phi_a(\boldsymbol{x} \quad \boldsymbol{x}_I)C^{\mathsf{O}}_i(\boldsymbol{x}; \boldsymbol{x} \quad \boldsymbol{x}_I), \tag{26}$$

where $i = 1, ..., d$ where d is the dimension of the problem. A correction function is introduced composed of a linear combination of monomials:

$$C^{\mathsf{O}}_i(\boldsymbol{x}; \boldsymbol{x} \quad \boldsymbol{x}_I) = \boldsymbol{H}(\boldsymbol{x} \quad \boldsymbol{x}_I)^{\mathsf{I}} \boldsymbol{b}^{\mathsf{O}}_i(\boldsymbol{x}). \tag{27}$$

The implicit gradient is then obtained by enforcing the gradient reproducing conditions (25) on (26) an solving for $\boldsymbol{b}^{\mathsf{O}}_i(\boldsymbol{x})$:

$$\Psi^{\mathsf{O}}_{Ii}(\boldsymbol{x}) = \left[\boldsymbol{H}^{\mathsf{O}}_i\right]^{\mathsf{I}} \boldsymbol{M}(\boldsymbol{x}) \quad ^1\boldsymbol{H}(\boldsymbol{x} \quad \boldsymbol{x}_I)\Phi_a(\boldsymbol{x} \quad \boldsymbol{x}_I) \tag{28}$$

where $\boldsymbol{M}(\boldsymbol{x})$ is the same moment matrix in (21), and $\boldsymbol{H}^{\mathsf{O}}_i$ is a column vector of the form:

$$\boldsymbol{H}^{\mathsf{O}}_i = [0, \quad , 0, \quad 1, 0, \quad , 0]^{\mathsf{I}} \tag{29}$$

where $\quad 1$ is $(i+1)^{th}$ entry. Compared to (23) it is easily seen that the implicit gradient (28) is much more computationally efficient. In fact, comparing (28) to (22), it costs virtually nothing since most of the terms already need to be computed in (22) — the last three terms are the exact same. Meanwhile, both possess the key property of satisfying the gradient reproducing conditions. Depending on the dimension of the problem d, the implicit gradient can reduce cost by a factor on the order of $2d + 1$ over the explicit gradient in the shape function construction [24]. In the later sections, the implicit gradient will be utilized to reduce the computational cost of the proposed nodal integration technique.

4 Instability in nodal integration

In meshfree methods, direct nodal integration (or DNI) is well known to provide unstable results in solid mechanics [2, 14, 15, 24, 64]. Here, we examine the stability of DNI in thermomechanical analysis using quasi-static classical thermoelasticity (neglecting inertial terms in (12)) as a model problem.

Consider a linear elastic half-space y 0 subjected to a sudden temperature change and free traction on its boundary. This can be treated as a one-dimensional problem, either coupled or uncoupled depending on the constants. The material properties employed in this study are shown in Table 1.

	k	ρ	c_p	β	$\lambda + 2\mu$
value	1.7 10^3	7.82 10 ^{3}	4.61 10^6	3.34 10^4	1.99 10^9
unit	kg cm/K/s^3	kg/cm^3	cm^2/K/s^3	kg/cm/K/s^2	kg/cm/s^2

Table 1: Parameters for stability study.

For constructing the RK shape function, linear basis, cubic B-spline kernel, uniform node distribution with spacing $\Delta x = 0.001$, and a normalized support size of 2 are used. The analytical solution for this problem can be found in [7]. The implicit and unconditionally stable backward difference method [48] with the time step $\Delta t = 0.001$s is used to discretize the time domain in this example.

Figure 1 shows the dimensionless results along the y-axis at time $\bar{t} = 2$ for the coupled ($\delta = 1$) and uncoupled ($\delta = 0$) cases. It can be seen that DNI yields highly unstable temperature and displacement responses. It should be emphasized that these oscillations are many orders of magnitude (more than 30 here) worse than those observed in pure elasticity (see [2, 22, 64] for a few examples, these instabilities in elasticity typically result in oscillations with amplitude on the order of the solution itself, or less). Hence here, stabilization is absolutely necessary to obtain any meaningful solution at all. It can also be seen that this severe instability occurs in both the coupled and uncoupled cases.

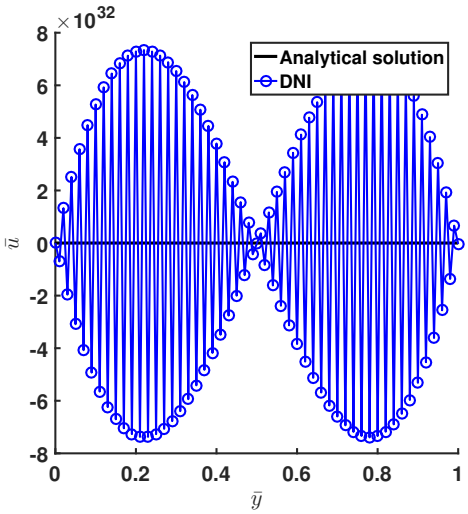

(a) Displacement: $\delta = 0$

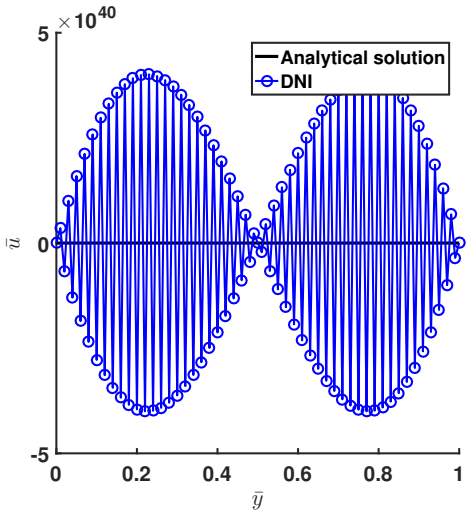

(b) Displacement: $\delta = 1$

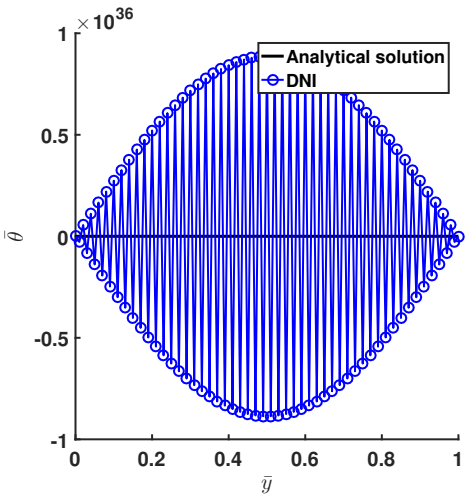

(c) Temperature change: $\delta = 0$

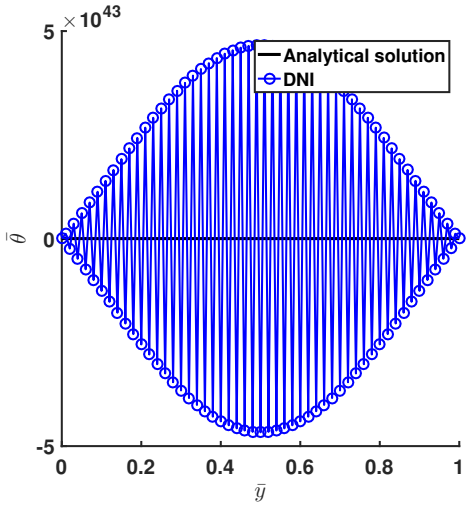

(d) Temperature change: $\delta = 1$

Figure 1: Coupled and uncoupled results along $\bar{y}$ at $\bar{t} = 2$ for the quasi-static DNI test.

The time histories at $\bar{y} = 1$ shown in Figure 2 depict the evolution of displacement and temperature difference over time. Here it can be seen that this instability is "explosive" in nature: the results appear to grow exponentially, which again is not the case in pure elasticity. As before, this occurs for both the coupled and uncoupled cases.

As explained in the introduction, DNI also provides poor accuracy. However, without stability, it is difficult to evaluate how the poor accuracy might manefest in this class of problems. Later, this issue will be revisited, where it is shown that stabilization alone (e.g., NSNI introduced in the next section) is insufficient to ensure acceptable accuracy, which motivates the introduction of variationally consistent NSNI (VC-NSNI), to attain both stability and accuracy in the solution of thermomechanical problems.

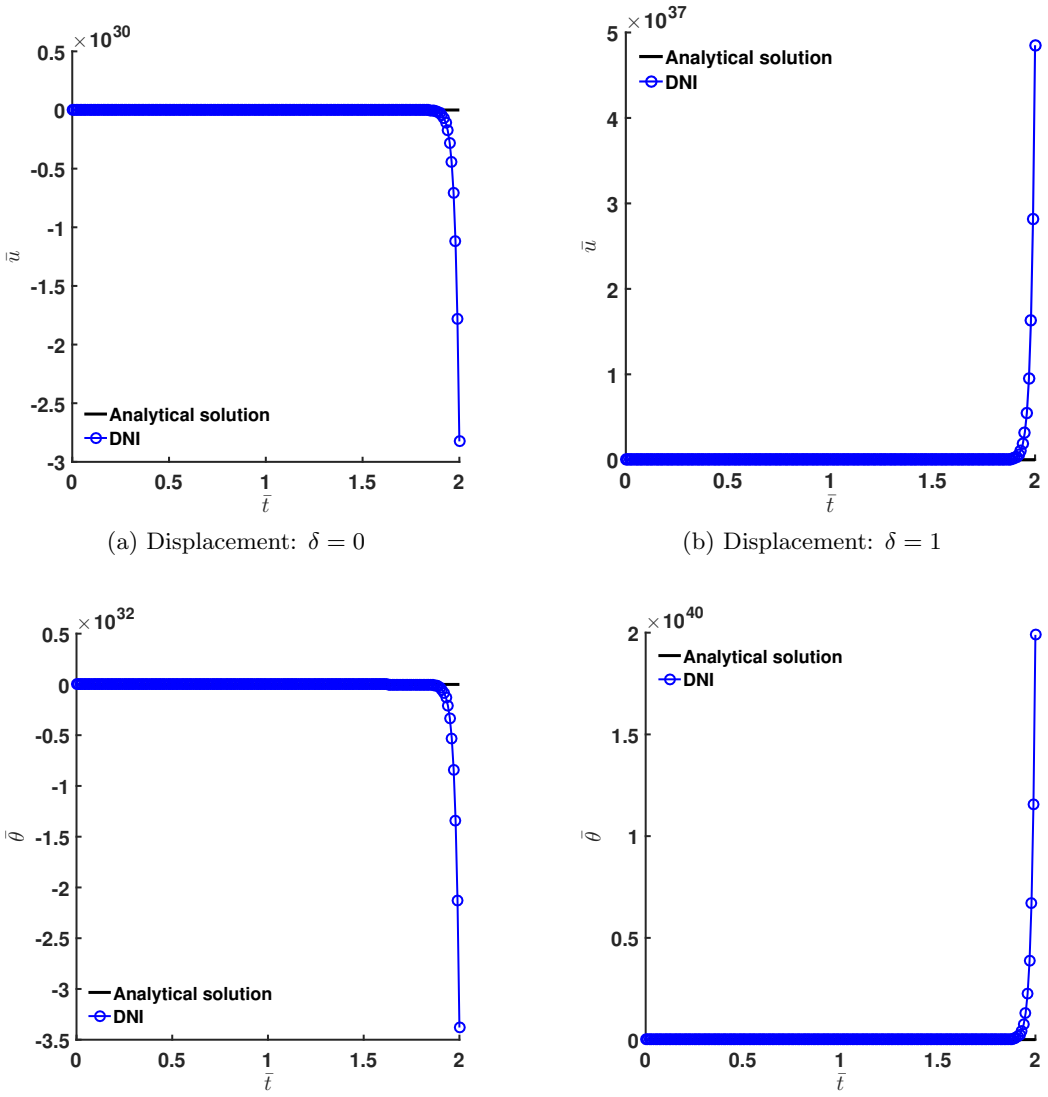

(a) Displacement: $\delta = 0$

(b) Displacement: $\delta = 1$

(c) Temperature change: $\delta = 0$

(d) Temperature change: $\delta = 1$

Figure 2: Coupled and uncoupled time history of results at $\bar{y} = 1$ for the quasi-static DNI test.

5 Naturally stabilized nodal integration

As shown in the previous section, the DNI quadrature scheme can lead to severe numerical instabilities and does not appear to be a viable scheme for thermomechanical problems whatsoever. To eliminate the spurious oscillatory modes of direct nodal integration, naturally stabilized nodal integration (NSNI) [24] has been introduced. However, this technique has not been developed for thermomechanical problems. Without loss of generality, two-dimensional formulations are presented in the following sections which can be easily extended or contracted to 3-d or 1-d.

5.1 Stabilization of the displacement field

To start, the strains in nodal domains Ω_L are expanded about the nodal position $\boldsymbol{x}_L$ using a Taylor series expansion truncated to first order [24]:

$$\boldsymbol{\varepsilon}(\boldsymbol{u}^h) \quad \boldsymbol{\varepsilon}_L(\boldsymbol{u}^h) + \sum_{i=1}^{2} \mathsf{f}(x_i \quad x_{Ii})\boldsymbol{\varepsilon}_L(\boldsymbol{u}^h)_{,i}\mathsf{g} \tag{30}$$

where $\boldsymbol{\varepsilon}_L(\boldsymbol{u}^h) \quad \boldsymbol{\varepsilon}(\boldsymbol{u}^h(\boldsymbol{x}_L))$. The strain of the test function is also defined the same as (30), that is

$$\boldsymbol{\varepsilon}(\boldsymbol{v}^h) \quad \boldsymbol{\varepsilon}_L(\boldsymbol{v}^h) + \sum_{i=1}^{2} \mathsf{f}(x_i \quad x_{Ii})\boldsymbol{\varepsilon}_L(\boldsymbol{v}^h)_{,i}\mathsf{g}. \tag{31}$$

Here, we have considered the linear ($n = 1$) case and only retain first-order terms. Higher order cases of NSNI can be obtained straightforwardly following [44].

Substituting (30) and (31) into (14a) for each of the strains in the nodal domains and employing the implicit gradient approximation (28), the following naturally stabilized nodal quadrature version of the elastic bilinear form is obtained as:

$$a_{DN}\left\langle \boldsymbol{v}^h, \boldsymbol{u}^h \right\rangle = a_D\left\langle \boldsymbol{v}^h, \boldsymbol{u}^h \right\rangle + a_N\left\langle \boldsymbol{v}^h, \boldsymbol{u}^h \right\rangle \tag{32}$$

where $a_D\,\mathsf{h}\,,\ \mathsf{i}$ is the DNI quadrature version of the bilinear form:

$$a_D\left\langle \boldsymbol{v}^h, \boldsymbol{u}^h \right\rangle = \sum_{L=1}^{NP} \boldsymbol{\varepsilon}_L(\boldsymbol{v}^h) : \mathsf{C} : \boldsymbol{\varepsilon}_L(\boldsymbol{u}^h) W_L \tag{33}$$

where W_L is the integration weight associated with node L (the representative nodal area in 2-d), and the stabilization term $a_N\,\mathsf{h}\,,\ \mathsf{i}$ is

$$a_N\left\langle \boldsymbol{v}^h, \boldsymbol{u}^h \right\rangle = \sum_{L=1}^{NP} \sum_{i=1}^{2} \hat{\boldsymbol{\varepsilon}}_{Li}(\boldsymbol{v}^h) : \mathsf{C} : \hat{\boldsymbol{\varepsilon}}_{Li}(\boldsymbol{u}^h) M_{Li} \tag{34}$$

where $\hat{\boldsymbol{\varepsilon}}_{Li}(\ )$ is the implicit gradient approximation of $\boldsymbol{\varepsilon}_L(\ )_{,i}$, and

$$M_{Li} = \int_{\Omega_L} (x_i \quad x_{Li})^2 \, d\Omega, \tag{35}$$

which are the second moments of inertia of each integration zone. Note that the following (in 2-D, see [24] for more details on this assumption) has been utilized to obtain (34):

$$\int_{\Omega_L} (x_1 \quad x_{L1})\, dx_1 = 0, \quad \text{or} \quad \int_{\Omega_L} (x_2 \quad x_{L2})\, dx_2 = 0. \tag{36}$$

The assumption (36) is satisfied when the node is located at the centroid of the quadrature domain Ω_L in at least one of the two Cartesian coordinates.

Using Voigt notation (for such terms throughout the manuscript), the standard nodal strain terms in (33) are constructed as:

$$\boldsymbol{\varepsilon}_L(\boldsymbol{u}^h) = \sum_{I=1}^{NP} \boldsymbol{B}_I^u(\boldsymbol{x}_L)\boldsymbol{u}_I, \quad \boldsymbol{\varepsilon}_L(\boldsymbol{v}^h) = \sum_{I=1}^{NP} \boldsymbol{B}_I^u(\boldsymbol{x}_L)\boldsymbol{v}_I, \tag{37}$$

with

$$\boldsymbol{B}_I^u(\boldsymbol{x}) = \begin{bmatrix} \Psi_{I,1}(\boldsymbol{x}) & 0 \\ 0 & \Psi_{I,2}(\boldsymbol{x}) \\ \Psi_{I,2}(\boldsymbol{x}) & \Psi_{I,1}(\boldsymbol{x}) \end{bmatrix}. \tag{38}$$

and the additional terms the containing derivatives of strains are approximated by implicit gradients (28) as

$$\begin{aligned} &\hat{\boldsymbol{\varepsilon}}_{Li}(\boldsymbol{u}^h) = \sum_{I=1}^{NP} \boldsymbol{B}_{Ii}^{u\mathsf{O}}(\boldsymbol{x}_L)\boldsymbol{u}_I \quad \boldsymbol{B}_i^{u\mathsf{O}}(\boldsymbol{x}_L)\boldsymbol{u}, \quad \hat{\boldsymbol{\varepsilon}}_{Li}(\boldsymbol{v}^h) = \sum_{I=1}^{NP} \boldsymbol{B}_{Ii}^{u\mathsf{O}}(\boldsymbol{x}_L)\boldsymbol{v}_I \quad \boldsymbol{B}_i^{u\mathsf{O}}(\boldsymbol{x}_L)\boldsymbol{v}, \\ &\boldsymbol{B}_{Ii}^{u\mathsf{O}}(\boldsymbol{x}) = \begin{bmatrix} \Psi_{Ii1}^{\mathsf{O}}(\boldsymbol{x}) & 0 \\ 0 & \Psi_{Ii2}^{\mathsf{O}}(\boldsymbol{x}) \\ \Psi_{Ii2}^{\mathsf{O}}(\boldsymbol{x}) & \Psi_{Ii1}^{\mathsf{O}}(\boldsymbol{x}) \end{bmatrix} \end{aligned} \tag{39}$$

where $\Psi_{Iij}^{\mathsf{O}} = \frac{1}{2}\left(\Psi_{Ii,j}^{\mathsf{O}} + \Psi_{Ij,i}^{\mathsf{O}}\right)$ since $\Psi_{Ii,j}^{\mathsf{O}} \neq \Psi_{Ij,i}^{\mathsf{O}}$.

5.2 Stabilization of temperature field

Following the stabilization of the displacement field, expanding the temperature gradient in nodal domains Ω_L about $\boldsymbol{x}_L$ is proposed in this work to achieve stabilization of the temperature field:

$$\mathsf{r}\,\theta^h(\boldsymbol{x}) \quad \mathsf{r}\,\theta_L^h + \sum_{i=1}^{2} \left(x_i \quad x_{Ii}\right)\left(\mathsf{r}\,\theta_L^h\right)_{,i} \tag{40}$$

where $\mathsf{r}\,\theta_L^h \quad \mathsf{r}\,\theta^h(\boldsymbol{x}_L)$. The test function gradient follows the same form:

$$\mathsf{r}\,S^h(\boldsymbol{x}) \quad \mathsf{r}\,S_L^h + \sum_{i=1}^{2} \left(x_i \quad x_{Ii}\right)\left(\mathsf{r}\,S_L^h\right)_{,i} \tag{41}$$

where $\mathsf{r}\,S_L^h \quad \mathsf{r}\,S^h(\boldsymbol{x}_L)$. Note that for the temperature field, stabilization also entails second-order derivatives, which are expensive to compute in meshfree approximations. Here, implicit gradients will again be introduced to approximate the derivatives of the temperature gradients.

Taking equations (35) and (36) into consideration, and employing (40) and (41) in (14b), the following stabilized bilinear form is obtained for the temperature field:

$$\bar{a}_{DN} < S^h, \theta^h >= \bar{a}_D < S^h, \theta^h > + \bar{a}_N < S^h, \theta^h > \tag{42}$$

where $\bar{a}_D < \ , \ >$ is the DNI quadrature version of the bilinear form:

$$\bar{a}_N \left\langle S^h, \theta^h \right\rangle = \sum_{L=1}^{NP} k(\mathsf{r}\,S_L^h) \quad (\mathsf{r}\,\theta_L^h) W_L \tag{43}$$

and the stabilization term for temperature $\bar{a}_N \mathsf{h}\ ,\ \mathsf{i}$ is computed as

$$\bar{a}_N \left\langle S^h, \theta^h \right\rangle = \sum_{L=1}^{NP} \sum_{i=1}^{2} k(\hat{\mathsf{r}}\,S_{Li}^h) \quad (\hat{\mathsf{r}}\,\theta_{Li}^h) M_{Li}. \tag{44}$$

where $\hat{r}\, S^h_{Li}$ and $\hat{r}\, \theta^h_{Li}$ denote the implicit derivative in the i^{th} direction of $r\, S^h_L$ and $r\, \theta^h_L$, respectively.

For the nodal gradients in the DNI term, we have:

$$r\, \theta^h_L = \sum_{I=1}^{NP} \boldsymbol{B}^{\theta}_I(\boldsymbol{x}_L)\theta_I, \quad r\, S^h_L = \sum_{I=1}^{NP} \boldsymbol{B}^{\theta}_I(\boldsymbol{x}_L) S_I, \tag{45}$$

where

$$\boldsymbol{B}^{\theta}_I(\boldsymbol{x}) = \begin{bmatrix} \Psi_{I,1}(\boldsymbol{x}) & \Psi_{I,2}(\boldsymbol{x}) \end{bmatrix}^{\mathsf{I}}. \tag{46}$$

For the stabilization terms in (44), implicit gradients are utilized as follows:

$$\begin{aligned} &\hat{r}\, \theta^h_{Li} = \sum_{I=1}^{NP} \boldsymbol{B}^{\theta\mathsf{O}}_{Ii}(\boldsymbol{x}_L)\theta_I \quad \boldsymbol{B}^{\theta\mathsf{O}}_{i}(\boldsymbol{x}_L)\boldsymbol{\theta}, \quad \hat{r}\, S^h_{Li} = \sum_{I=1}^{NP} \boldsymbol{B}^{\theta\mathsf{O}}_{Ii}(\boldsymbol{x}_L) S_I \quad \boldsymbol{B}^{\theta\mathsf{O}}_{i}(\boldsymbol{x}_L)\boldsymbol{S}, \\ &\boldsymbol{B}^{\theta\mathsf{O}}_{Ii}(\boldsymbol{x}) = \begin{bmatrix} \Psi^{\mathsf{O}}_{Ii1}(\boldsymbol{x}) & \Psi^{\mathsf{O}}_{Ii2}(\boldsymbol{x}) \end{bmatrix}^{\mathsf{I}}. \end{aligned} \tag{47}$$

Note that the weights W_L and second moments of inertia M_{Li} are the same as in Section 5.1.

6 Variational consistency conditions

In this section, the variational consistency conditions are derived for thermoelasticity. The key difference between the original derivation in [11] is the presence of two fields.

Following the concept in [11], consider a static thermoelasticity problem where the displacement solution is a linear combination of complete monomials up to order n:

$$\boldsymbol{u} = \sum_{j\alpha j\ \ n} \boldsymbol{c}_\alpha \boldsymbol{x}^\alpha \quad \boldsymbol{u}^{[n]} \tag{48}$$

where α is a multi-index equipped with standard notation.

In [11], the conditions to obtain this type of solution was purely a function of the single field. Here we note that, unlike the pure elastic case, the associated boundary conditions now also need to consider the temperature change since, e.g., the prescribed traction will need to depend on $\boldsymbol{\sigma} = \mathsf{C} : \boldsymbol{\varepsilon}(\boldsymbol{u}) \quad \beta\theta\mathsf{I}$. In addition, the temperature change needs to be considered an independent variable. As such, an mth order temperature solution is assumed:

$$\theta = \sum_{j\gamma j\ \ m} d_\gamma x^\gamma \quad \theta^{[m]} \tag{49}$$

where γ is also a multi-index. With (48) and (49) in hand, the manufactured source term and boundary conditions consistent with these two fields can now be obtained as:

$$\boldsymbol{b} = \quad r \quad \boldsymbol{\sigma}^{[nm]} \qquad \text{in } \Omega \tag{50a}$$

$$\boldsymbol{h} = \boldsymbol{\sigma}^{[nm]} \quad \boldsymbol{n} \qquad \text{on } \partial\Omega_h \tag{50b}$$

$$\boldsymbol{g} = \mathbf{u}^{[n]} \qquad \text{on } \partial\Omega_g \tag{50c}$$

$$Q = \quad r \quad k\, r\, \theta^{[m]} \qquad \text{in } \Omega \tag{50d}$$

$$\bar{q} = k\, r\, \theta^{[m]} \quad \boldsymbol{n} \qquad \text{on } \partial\Omega_q \tag{50e}$$

$$\bar{\theta} = \theta^{[m]} \qquad \text{on } \partial\Omega_T. \tag{50f}$$

where

$$\boldsymbol{\sigma}^{[nm]} = \mathsf{C} : \boldsymbol{\varepsilon}(\boldsymbol{u}^{[n]}) \quad \beta\theta^{[m]}\mathsf{I} \tag{51}$$

is the stress associated with both fields.

For the Galerkin form, approximations for both solid displacement and temperature fields are as follows

$$\boldsymbol{u}^h = \sum_{I=1}^{NP} \boldsymbol{N}_I^u \boldsymbol{u}_I, \quad \theta^h = \sum_{I=1}^{NP} \bar{\Psi}_I \theta_I \tag{52}$$

where

$$\boldsymbol{N}_I^u = \begin{bmatrix} \Psi_I & 0 \\ 0 & \Psi_I \end{bmatrix}, \tag{53}$$

and the test functions are

$$\boldsymbol{v}^h = \sum_{I=1}^{NP} \hat{\boldsymbol{N}}_I^u \boldsymbol{v}_I, \quad S^h = \sum_{I=1}^{NP} \tilde{\Psi}_I S_I \tag{54}$$

where

$$\hat{\boldsymbol{N}}_I^u = \begin{bmatrix} \hat{\Psi}_I & 0 \\ 0 & \hat{\Psi}_I \end{bmatrix}, \tag{55}$$

in which Ψ, $\bar{\Psi}$, $\hat{\Psi}$, and $\tilde{\Psi}$ are the RK shape functions for solid displacement and temperature fields, respectively, and $\boldsymbol{u}_I$, θ_I, $\boldsymbol{v}_I$, and S_I are the nodal coefficients.

Now, in order to obtain Galerkin exactness (passing the patch test and obtaining the exact solutions (48) and (49)), the integration constraints should be satisfied. The meaning of integration constraints is that the numerical integration has to be consistent with the test functions in order to obtain exactness in the Galerkin approximation. Therefore here, the possibility that approximations to the test and trial functions differ is considered. Note that the integration constraints are tightly tied with Galerkin orthogonality [52], and are necessary for obtaining the standard error estimate for smooth problems [66].

In order to arrive at the integration constraints, weak forms employed in the Galerkin equation must attest to the strong forms [11]. A few options are the Lagrange multiplier method, Nitsche's method, or the newly proposed *consistent weak forms* [28]. Here we consider the consistent weak forms of (12) — the details are omitted here for clarity. The derivation follows the appendices of [28] straightforwardly.

Since the test functions are arbitrary, one governing equation can be considered at a time. Therefore, one should expect two independent constraints for each test function approximation.

First, consider the equation of motion. Following [11], the approximations (52) and (54) are substituted into the consistent versions of (14a) and (14b). Then, using the notation $\boldsymbol{x}_I^\alpha \quad x_{I1}^{\alpha_1} \; x_{I2}^{\alpha_2} \; \ldots \; x_{Id}^{\alpha_d}$, the exact nodal solutions $\boldsymbol{u}_I^{[n]}$ and $\theta_I^{[m]}$ are then employed along with the consistency conditions (19) yielding $\boldsymbol{u}^h = \boldsymbol{u}^{[n]}$ and $\theta^h = \theta^{[m]}$. Using the prescribed conditions in (50), and employing numerical integration, the following integration constraints on the test function for the displacement field are obtained:

$$\left\langle r\,\hat{\Psi}_I \quad \boldsymbol{\sigma}^{[\alpha\gamma]} \right\rangle = \left\langle \hat{\Psi}_I\, r \quad \boldsymbol{\sigma}^{[\alpha\gamma]} \right\rangle + \left\langle \hat{\Psi}_I \boldsymbol{\sigma}^{[\alpha\gamma]} \quad \boldsymbol{n} \right\rangle_\partial \qquad \forall I, j\alpha j = 0, 1, \ldots, n, \quad j\gamma j = 0, 1, \ldots, m \tag{56}$$

where $\langle i$ and $\langle i_\partial$ denote the quadrature forms of the domain integral and the boundary integral, respectively, and $\boldsymbol{\sigma}^{[\alpha\gamma]} = \mathbb{C} : \boldsymbol{\varepsilon}(\boldsymbol{u}^\alpha) \quad \beta\theta^\gamma \mathbb{I}$. In the above, it can be seen that the integration constraint is the same as pure elasticity in terms of stress [11]. However here, the stress is a function of both displacement and temperature. Therefore the definition of $\boldsymbol{\sigma}^{[\alpha\gamma]}$ must be used to further elucidate the constraints:

$$\left\langle r^{\,s}\hat{\Psi}_I : \mathbb{C} : r^{\,s}\boldsymbol{x}^\alpha \right\rangle = \left\langle \hat{\Psi}_I\, r \quad \mathbb{C} : r^{\,s}\boldsymbol{x}^\alpha \right\rangle + \left\langle \hat{\Psi}_I \mathbb{C} : r^{\,s}\boldsymbol{x}^\alpha \quad \boldsymbol{n} \right\rangle_\partial \qquad \forall I, j\alpha j = 0, 1, \ldots, n \tag{57a}$$

$$\left\langle r^{\,s}\hat{\Psi}_I \quad \beta x^\gamma \mathbb{I} \right\rangle = \left\langle \hat{\Psi}_I\, r \quad \beta x^\gamma \mathbb{I} \right\rangle + \left\langle \hat{\Psi}_I \beta x^\gamma \mathbb{I} \quad \boldsymbol{n} \right\rangle_\partial \qquad \forall I, j\gamma j = 0, 1, \ldots, m \tag{57b}$$

where $r^{\,s}(\,) = \frac{1}{2}(r \quad (\,) + (\,) \quad r)$.

Remark 1 The above convey a relation between the displacement test functions, quadrature, and both orders of monomials of the solution n and m. This is due to the fact that the stress in the momentum equation contains both the displacement and the temperature difference.

Now, if C and β are constant, the constraint can be simplified as:

$$\left\langle r^{\,s}\hat{\Psi}_I \quad r^{\,s}\boldsymbol{x}^{\alpha} \right\rangle = \left\langle \hat{\Psi}_I\, r \quad r^{\,s}\boldsymbol{x}^{\alpha} \right\rangle + \left\langle \hat{\Psi}_I\, r^{\,s}\boldsymbol{x}^{\alpha} \quad \boldsymbol{n} \right\rangle_{\partial} \qquad \forall I, j\alpha j = 0, 1, \ldots, n \tag{58a}$$

$$\left\langle r^{\,s}\hat{\Psi}_I \quad x^{\gamma}\mathsf{I} \right\rangle = \left\langle \hat{\Psi}_I\, r \quad x^{\gamma}\mathsf{I} \right\rangle + \left\langle \hat{\Psi}_I x^{\gamma}\mathsf{I} \quad \boldsymbol{n} \right\rangle_{\partial} \qquad \forall I, j\gamma j = 0, 1, \ldots, m. \tag{58b}$$

Now considering the static energy equation, the integration constraints on the test function of the temperature field can be obtained following the previous procedure and assuming constant k:

$$\left\langle r\,\tilde{\Psi}_I \quad r\,x^{\gamma} \right\rangle = \left\langle \tilde{\Psi}_I\, r^{\,2} x^{\gamma} \right\rangle + \left\langle \tilde{\Psi}_I\, r\, x^{\gamma} \quad \boldsymbol{n} \right\rangle_{\partial} \qquad \forall I, j\gamma j = 0, 1, \ldots, m \tag{59}$$

where $r^{\,2} \quad r \quad r$.

Remark 2 Here it can be seen that this integration constraint only depends on the variable m, rather than a dependence on both n and m in the displacement constraint (57). This is due to the independence of $\boldsymbol{u}$ and θ in the energy equation in the static case.

To take an example of the specific constraints, consider linear fields of both temperature and displacement with $n = m = 1$. The following conditions on the displacement test function $\hat{\Psi}_I$ can be straightforwardly obtained by taking the various cases of α and γ up to length one in (57). In two dimensions, this yields:

$$\left\langle \hat{\Psi}_{I,j} \right\rangle = \left\langle \hat{\Psi}_I n_j \right\rangle_{\partial} \quad , \quad j = 1, 2 \quad \forall I \tag{60a}$$

$$\left\langle \hat{\Psi}_{I,2x_1} \right\rangle = \left\langle \hat{\Psi}_I x_1 n_2 \right\rangle_{\partial} \qquad \forall I \tag{60b}$$

$$\left\langle \hat{\Psi}_{I,1x_2} \right\rangle = \left\langle \hat{\Psi}_I x_2 n_1 \right\rangle_{\partial} \qquad \forall I \tag{60c}$$

$$\left\langle \hat{\Psi}_{I,1x_1} \right\rangle = \left\langle \hat{\Psi}_I \right\rangle + \left\langle \hat{\Psi}_I x_1 n_1 \right\rangle_{\partial} \qquad \forall I \tag{60d}$$

$$\left\langle \hat{\Psi}_{I,2x_2} \right\rangle = \left\langle \hat{\Psi}_I \right\rangle + \left\langle \hat{\Psi}_I x_2 n_2 \right\rangle_{\partial} \qquad \forall I. \tag{60e}$$

And in three dimensions, one obtains:

$$\left\langle \hat{\Psi}_{I,j} \right\rangle = \left\langle \hat{\Psi}_I n_j \right\rangle_{\partial} \quad , \quad j = 1, 2, 3 \quad \forall I \tag{61a}$$

$$\left\langle \hat{\Psi}_{I,jx_1} \right\rangle = \left\langle \hat{\Psi}_I x_1 n_j \right\rangle_{\partial} \quad , \quad j = 2, 3 \quad \forall I \tag{61b}$$

$$\left\langle \hat{\Psi}_{I,jx_2} \right\rangle = \left\langle \hat{\Psi}_I x_2 n_j \right\rangle_{\partial} \quad , \quad j = 1, 3 \quad \forall I \tag{61c}$$

$$\left\langle \hat{\Psi}_{I,jx_3} \right\rangle = \left\langle \hat{\Psi}_I x_3 n_j \right\rangle_{\partial} \quad , \quad j = 1, 2 \quad \forall I \tag{61d}$$

$$\left\langle \hat{\Psi}_{I,1x_1} \right\rangle = \left\langle \hat{\Psi}_I \right\rangle + \left\langle \hat{\Psi}_I x_1 n_1 \right\rangle_{\partial} \qquad \forall I \tag{61e}$$

$$\left\langle \hat{\Psi}_{I,2x_2} \right\rangle = \left\langle \hat{\Psi}_I \right\rangle + \left\langle \hat{\Psi}_I x_2 n_2 \right\rangle_{\partial} \qquad \forall I \tag{61f}$$

$$\left\langle \hat{\Psi}_{I,3x_3} \right\rangle = \left\langle \hat{\Psi}_I \right\rangle + \left\langle \hat{\Psi}_I x_3 n_3 \right\rangle_{\partial} \qquad \forall I. \tag{61g}$$

For the energy equation, the constraint on the test function for temperature change $\tilde{\Psi}_I$ can be shown to have the following form using $j\gamma j = 0, 1$:

$$\left\langle r\,\tilde{\Psi}_I \right\rangle = \left\langle \tilde{\Psi}_I \boldsymbol{n} \right\rangle_{\partial} \quad \forall I. \tag{62}$$

Remark 3 Satisfaction of the constraints associated with the displacement test function implies (62) as seen in (60a) and (61a). Therefore, if a single test function is used for both fields, then the displacement constraint can be employed for satisfaction of variational consistency uniformly up to order $m = n$.

Remark 4 In thermoelasticity, the linear constraints are less trivial than in elasticity. However as will be seen, the corrections can still be constructed in a simple manner.

Remark 5 It can be shown that the use of naturally stabilized nodal integration results in the same constraints as derived herein for the linear case. Therefore, the techniques in the following section can be straightforwardly applied for $n = 1$. The derivation follows [24] — if a linear field is assumed in (48) and (49), gradients are constant, and the derivative of gradients in NSNI stabilization terms are zero and drop out of the variational consistency conditions.

Remark 6 Here, as in all other works based on variationally consistent integration, we have only considered a monomial distribution of a solution distributed in space, constant in time. Therefore dynamic terms are not considered. Nevertheless, as shown in [27], it was clearly demonstrated via numerical examples that satisfaction of these static conditions significantly improves the response in a dynamic setting. In addition, it was shown in [52, 66] that this condition is necessary in order to obtain the standard error estimates (optimal rates for smooth problems) and restore Galerkin orthogonality.

7 Variationally consistent integration for thermoelasticity

Satisfaction of (60) and (62) can be achieved by modifying the shape function gradient of the test function in the following from [25]:

$$\nabla \Psi_I^c(\boldsymbol{x}) = \nabla \Psi_I(\boldsymbol{x}) + R_I(\boldsymbol{x}) \begin{Bmatrix} \zeta_{I1} \\ \zeta_{I2} \end{Bmatrix} + R_I(\boldsymbol{x}) \begin{pmatrix} x_1 & x_{1I} \end{pmatrix} \begin{Bmatrix} \zeta_{I3} \\ \zeta_{I4} \end{Bmatrix} + R_I(\boldsymbol{x}) \begin{pmatrix} x_2 & x_{2I} \end{pmatrix} \begin{Bmatrix} \zeta_{I5} \\ \zeta_{I6} \end{Bmatrix} \tag{63}$$

where

$$R_I(\boldsymbol{x}) = \begin{cases} 1, & \text{if } \boldsymbol{x} \in \text{supp}(\Psi_I) \\ 0, & \text{if } \boldsymbol{x} \notin \text{supp}(\Psi_I) \end{cases} \tag{64}$$

where $\text{supp}(\Psi_I)$ denotes the support of Ψ_I. Substitution of (63) into (60) results in two systems of equations:

$$\mathbf{A}_I \boldsymbol{\zeta}_I^{c1} = \mathbf{r}_I^{c1} \tag{65a}$$

$$\mathbf{A}_I \boldsymbol{\zeta}_I^{c2} = \mathbf{r}_I^{c2} \tag{65b}$$

where

$$\mathbf{A}_I = \int \boldsymbol{P}(\boldsymbol{x} - \boldsymbol{x}_I) \boldsymbol{P}^{\mathsf{T}}(\boldsymbol{x} - \boldsymbol{x}_I) R_I(\boldsymbol{x}) \, d \tag{66a}$$

$$\boldsymbol{P}(\boldsymbol{x}) = \{1, x_1, x_2\}^{\mathsf{T}} \tag{66b}$$

$$\boldsymbol{\zeta}_I^{c1} = \{\zeta_{I1}, \zeta_{I3}, \zeta_{I5}\}^{\mathsf{T}} \tag{66c}$$

$$\boldsymbol{\zeta}_I^{c2} = \{\zeta_{I2}, \zeta_{I4}, \zeta_{I6}\}^{\mathsf{T}} \tag{66d}$$

$$\mathbf{r}_I^{c1} = \left\{ r_{I1}^1, r_{I1}^2, r_{I1}^3 \right\}^{\mathsf{T}} \tag{66e}$$

$$\mathbf{r}_I^{c2} = \left\{ r_{I2}^1, r_{I2}^2, r_{I2}^3 \right\}^{\mathsf{T}} \tag{66f}$$

and

$$r^1_{I1} = \hbar\Psi_I n_1 \imath_\partial \quad \hbar\Psi_{I,1}\imath \tag{67a}$$
$$r^1_{I2} = \hbar\Psi_I n_2 \imath_\partial \quad \hbar\Psi_{I,2}\imath \tag{67b}$$
$$r^2_{I1} = \hbar\Psi_I n_1 (x_1 \quad x_{1I})\imath_\partial \quad \hbar\Psi_I \imath \quad \hbar\Psi_{I,1}(x_1 \quad x_{1I})\imath \tag{67c}$$
$$r^2_{I2} = \hbar\Psi_I n_2 (x_1 \quad x_{1I})\imath_\partial \quad \hbar\Psi_{I,2}(x_1 \quad x_{1I})\imath \tag{67d}$$
$$r^3_{I1} = \hbar\Psi_I n_1 (x_2 \quad x_{2I})\imath_\partial \quad \hbar\Psi_{I,1}(x_2 \quad x_{2I})\imath \tag{67e}$$
$$r^3_{I2} = \hbar\Psi_I n_2 (x_2 \quad x_{2I})\imath_\partial \quad \hbar\Psi_I \imath \quad \hbar\Psi_{I,2}(x_2 \quad x_{2I})\imath \quad . \tag{67f}$$

Due to the locality of $R_I(\boldsymbol{x})$, and dependence on the nodal index I, the residuals (67) and correction terms (66) are relatively computationally inexpensive. In [24, 26] it was shown that the VC correction of nodal integration only slightly increases computational cost, and is far more effective than several other types of nodal integration in terms of CPU time for a given level of error achieved, and vice versa.

8 Space discretization and time integration scheme

8.1 Approximations

As previously mentioned, the VC scheme can be uniformly applied to both sets of test functions. Here, we also use the same set of trial functions for both fields. As a result, the approximation of displacement and temperature change are constructed as:

$$\boldsymbol{u}^h(\boldsymbol{x}) = \sum_{I=1}^{NP} \boldsymbol{N}_I(\boldsymbol{x})\boldsymbol{u}_I \quad \mathbf{N}(\boldsymbol{x})\boldsymbol{u}, \quad \theta^h(\boldsymbol{x}) = \sum_{I=1}^{NP} \Psi_I(\boldsymbol{x})\theta_I \quad \boldsymbol{\Psi}(\boldsymbol{x})\boldsymbol{\theta} \tag{68}$$

where

$$\boldsymbol{N}_I(\boldsymbol{x}) = \begin{bmatrix} \Psi_I(\boldsymbol{x}) & 0 \\ 0 & \Psi_I(\boldsymbol{x}) \end{bmatrix}, \tag{69}$$

and the test functions are approximated as

$$\boldsymbol{v}^h(\boldsymbol{x}) = \sum_{I=1}^{NP} \boldsymbol{N}_I(\boldsymbol{x})\boldsymbol{v}_I \quad \mathbf{N}(\boldsymbol{x})\boldsymbol{v}, \quad S^h(\boldsymbol{x}) = \sum_{I=1}^{NP} \Psi_I(\boldsymbol{x})S_I \quad \boldsymbol{\Psi}(\boldsymbol{x})\boldsymbol{S} \tag{70}$$

where $\{\Psi_I\}_{I=1}^{NP}$ are the RK shape functions (22), and $\boldsymbol{u}_I$, θ_I, $\boldsymbol{v}_I$, and S_I are the nodal coefficients in the Galerkin equation. Note that all approximations and assembly operations are carried out local to any integration point $\boldsymbol{x}$, that is, only over indices which are associated with non-zero shape functions at the location.

For the gradients, the assumed strain-type approach is adopted herein following [11], where the trial function terms are computed in a straightforward manner:

$$\varepsilon(\boldsymbol{u}^h(\boldsymbol{x})) = \sum_{I=1}^{NP} \boldsymbol{B}^u_I(\boldsymbol{x})\boldsymbol{u}_I \quad \mathbf{B}^u(\boldsymbol{x})\boldsymbol{u}, \quad \nabla\theta^h(\boldsymbol{x}) = \sum_{I=1}^{NP} \boldsymbol{B}^\theta_I(\boldsymbol{x})\theta_I \quad \mathbf{B}^\theta(\boldsymbol{x})\boldsymbol{\theta} \tag{71}$$

where

$$\begin{aligned} \boldsymbol{B}^u_I(\boldsymbol{x}) &= \begin{bmatrix} \Psi_{I,1}(\boldsymbol{x}) & 0 \\ 0 & \Psi_{I,2}(\boldsymbol{x}) \\ \Psi_{I,2}(\boldsymbol{x}) & \Psi_{I,1}(\boldsymbol{x}) \end{bmatrix}, \\ \boldsymbol{B}^\theta_I(\boldsymbol{x}) &= [\Psi_{I,1}(\boldsymbol{x}), \Psi_{I,2}(\boldsymbol{x})]^\mathsf{T}. \end{aligned} \tag{72}$$

and the test function terms are corrected using (63):

$$\boldsymbol{\varepsilon}(\boldsymbol{v}^h(\boldsymbol{x})) = \sum_{I=1}^{NP} \boldsymbol{B}_I^{uc}(\boldsymbol{x})\boldsymbol{v}_I \quad \mathbf{B}^{uc}(\boldsymbol{x})\boldsymbol{v}, \quad \nabla S^h(\boldsymbol{x}) = \sum_{I=1}^{NP} \boldsymbol{B}_I^{\theta c}(\boldsymbol{x})S_I \quad \mathbf{B}^{\theta c}(\boldsymbol{x})\boldsymbol{S} \tag{73}$$

where

$$\begin{aligned} \boldsymbol{B}_I^{uc}(\boldsymbol{x}) &= \begin{bmatrix} \Psi_{I,1}^c(\boldsymbol{x}) & 0 \\ 0 & \Psi_{I,2}^c(\boldsymbol{x}) \\ \Psi_{I,2}^c(\boldsymbol{x}) & \Psi_{I,1}(\boldsymbol{x}) \end{bmatrix}, \\ \boldsymbol{B}_I^{\theta c}(\boldsymbol{x}) &= [\Psi_{I,1}^c(\boldsymbol{x}), \Psi_{I,2}^c(\boldsymbol{x})]^{\mathsf{T}}. \end{aligned} \tag{74}$$

Remark 7 Since the the VC conditions (57) and (59) do not include natural boundary conditions, and the test function gradient correction (63)-(67) does not appear in the weak Galerkin enforcement of boundary conditions (14), the approach is easily applicable to complex engineering problems without special considerations. Similarly, NSNI methods expand gradient terms only in bilinear forms. Therefore, NSNI also need not be considered in any boundary conditions. For examples of the use of these approaches in more complex applications, see [1] or [61].

8.2 Semi-discrete matrix form

For the matrix forms, let the following subscript notation be adopted: u denotes the mechanical field, and θ denotes the thermal field. Introducing (68), (70), (71), and (73) into the Galerkin equation (14), and employing the naturally stabilized nodal integration technique introduced in Section 5, the matrix system in 2D is obtained as:

$$\begin{bmatrix} \mathbf{M}_{uu} & \mathbf{0} \\ \mathbf{0} & \mathbf{0} \end{bmatrix} \begin{bmatrix} \ddot{\boldsymbol{u}} \\ \ddot{\boldsymbol{\theta}} \end{bmatrix} + \begin{bmatrix} \mathbf{0} & \mathbf{0} \\ \mathbf{C}_{\theta u} & \mathbf{C}_{\theta\theta} \end{bmatrix} \begin{Bmatrix} \dot{\boldsymbol{u}} \\ \dot{\boldsymbol{\theta}} \end{Bmatrix} + \begin{bmatrix} \mathbf{K}_{uu} & \mathbf{K}_{u\theta} \\ \mathbf{0} & \mathbf{K}_{\theta\theta} \end{bmatrix} \begin{Bmatrix} \boldsymbol{u} \\ \boldsymbol{\theta} \end{Bmatrix} = \begin{Bmatrix} \mathbf{F}^{\mathsf{ext}} \\ \mathbf{Q}^{\mathsf{ext}} \end{Bmatrix} \tag{75}$$

where $\boldsymbol{u}$ and $\boldsymbol{\theta}$ are the row vectors of $\{\boldsymbol{u}_I\}_{I=1}^{NP}$ and $\{\theta_I\}_{I=1}^{NP}$, respectively, and for a homogeneous media as presented in the examples:

$$\mathbf{M}_{uu} = \sum_{L=1}^{NP} \rho \mathbf{N}(\boldsymbol{x}_L)^{\mathsf{T}} \mathbf{N}(\boldsymbol{x}_L) W_L \tag{76a}$$

$$\mathbf{C}_{\theta u} = T_0 \mathbf{K}_{u\theta}^{\mathsf{T}} \tag{76b}$$

$$\mathbf{C}_{\theta\theta} = \sum_{L=1}^{NP} \rho c_p \boldsymbol{\Psi}(\boldsymbol{x}_L)^{\mathsf{T}} \boldsymbol{\Psi}(\boldsymbol{x}_L) W_L \tag{76c}$$

$$\mathbf{K}_{uu} = \sum_{L=1}^{NP} (\mathbf{B}^{uc}(\boldsymbol{x}_L))^{\mathsf{T}} \mathbf{D} \mathbf{B}^{u}(\boldsymbol{x}_L) W_L + \sum_{L=1}^{NP} \sum_{i=1}^{2} (\mathbf{B}_i^{u\mathsf{O}}(\boldsymbol{x}_L))^{\mathsf{T}} \mathbf{D} \mathbf{B}_i^{u\mathsf{O}}(\boldsymbol{x}_L) M_{Li} \tag{76d}$$

$$\mathbf{K}_{u\theta} = \sum_{L=1}^{NP} \beta (\mathbf{B}^{uc}(\boldsymbol{x}_L))^{\mathsf{T}} \mathbf{I} \boldsymbol{\Psi}(\boldsymbol{x}_L) W_L \tag{76e}$$

$$\mathbf{K}_{\theta\theta} = \sum_{L=1}^{NP} k (\mathbf{B}^{\theta c}(\boldsymbol{x}_L))^{\mathsf{T}} \mathbf{B}^{\theta}(\boldsymbol{x}_L) W_L + \sum_{L=1}^{NP} \sum_{i=1}^{2} k (\mathbf{B}_i^{\theta\mathsf{O}}(\boldsymbol{x}_L))^{\mathsf{T}} \mathbf{B}_i^{\theta\mathsf{O}}(\boldsymbol{x}_L) M_{Li} \tag{76f}$$

$$\mathbf{F}^{\mathsf{ext}} = \sum_{L=1}^{NP} \mathbf{N}(\boldsymbol{x}_L)^{\mathsf{T}} \mathbf{b} W_L + \sum_{K=1}^{NBPu} \mathbf{N}(\boldsymbol{x}_K)^{\mathsf{T}} \mathbf{h} L_K^u \tag{76g}$$

$$\mathbf{Q}^{\mathsf{ext}} = \sum_{L=1}^{NP} \boldsymbol{\Psi}(\boldsymbol{x}_L)^{\mathsf{T}} Q W_L + \sum_{K=1}^{NBP\theta} \boldsymbol{\Psi}(\boldsymbol{x}_K)^{\mathsf{T}} \bar{q} L_K^{\theta} \tag{76h}$$

where $\mathbf{I} = \begin{bmatrix}1 & 1 & 0 & 0\end{bmatrix}^{\mathsf{I}}$, $\mathbf{D}$ is the matrix corresponding to the tensor C, $\mathbf{b}$ and $\mathbf{h}$ are the matrix forms of $\boldsymbol{b}$ and $\boldsymbol{h}$, respectively, L_K^u and L_K^θ denote the Kth weight of one of the $NBPu$ and $NBP\theta$ integration points on the natural boundaries for the displacement and temperature change, respectively, and $\mathbf{B}_i^{u\mathsf{O}}$ and $\mathbf{B}_i^{\theta\mathsf{O}}$ are the global matrices in (39) and (47), respectively.

The final semi-discrete linear time-dependent system (75) can be written in compact form as

$$\mathbf{M}\ddot{\mathbf{d}}(t) + \mathbf{C}\dot{\mathbf{d}}(t) + \mathbf{K}\mathbf{d}(t) = \mathbf{F}(t) \tag{77}$$

where

$$\mathbf{M} = \begin{bmatrix}\mathbf{M}_{uu} & \mathbf{0}\\ \mathbf{0} & \mathbf{0}\end{bmatrix}, \quad \mathbf{C} = \begin{bmatrix}\mathbf{0} & \mathbf{0}\\ \mathbf{C}_{\theta u} & \mathbf{C}_{\theta\theta}\end{bmatrix}, \quad \mathbf{K} = \begin{bmatrix}\mathbf{K}_{uu} & \mathbf{K}_{u\theta}\\ \mathbf{0} & \mathbf{K}_{\theta\theta}\end{bmatrix} \tag{78}$$

and

$$\mathbf{d} = \begin{bmatrix}\boldsymbol{u}\\ \boldsymbol{\theta}\end{bmatrix}, \quad \mathbf{F} = \begin{bmatrix}\mathbf{F}^{\mathsf{ext}}\\ \mathbf{Q}^{\mathsf{ext}}\end{bmatrix}. \tag{79}$$

8.3 Time integration

In this research, the semi-discrete equations are advanced in time using the Newmark method, which consists of the following equations [31]:

$$\mathbf{M}\mathbf{a}_{n+1} + \mathbf{C}\mathbf{v}_{n+1} + \mathbf{K}\mathbf{d}_{n+1} = \mathbf{F}_{n+1} \tag{80a}$$

$$\mathbf{d}_{n+1} = \mathbf{d}_n + \Delta t\mathbf{v}_n + \frac{\Delta t^2}{2}[(1 \quad 2\bar{\beta})\mathbf{a}_n + 2\bar{\beta}\mathbf{a}_{n+1}] \tag{80b}$$

$$\mathbf{v}_{n+1} = \mathbf{v}_n + \Delta t[(1 \quad \gamma)\mathbf{a}_n + \gamma\mathbf{a}_{n+1}] \tag{80c}$$

where $\mathbf{d}_n$, $\mathbf{v}_n$, and $\mathbf{a}_n$ are the approximations of $\mathbf{d}(t_n)$, $\dot{\mathbf{d}}(t_n)$, and $\ddot{\mathbf{d}}(t_n)$, respectively, and $\bar{\beta}$ and γ are the Newmark parameters.

9 Numerical examples

In this section numerical examples are presented to demonstrate the accuracy and stability of the proposed method. The following five numerical integration methods are tested for comparison:

1. Direct nodal integration (denoted DNI)
2. Variationally consistent integration with direct nodal integration (denoted VC-DNI)
3. Naturally stabilized nodal integration (denoted NSNI)
4. Variationally consistent integration with naturally stabilized nodal integration (denoted VC-NSNI)
5. Gaussian integration (denoted GI) with high order rules

Thermoelastic benchmarks are solved, and the solution by these approaches are compared with exact solutions and results from numerical methods in the literature.

Unless otherwise stated, for the RK approximation, linear basis with cubic B-spline kernels with a normalized support size of 2 are employed in all problems, using a uniform node distribution with a nodal spacing of $\Delta x = 0.001$. The five point Gaussian quadrature rule is used for GI with cell boundaries coincident with the nodal positions. The implicit and unconditionally stable backward difference method [48] is employed with a time step of $\Delta t = 0.001$ to discretize the time domain in all examples. The transformation method [12] is used for the imposition of essential boundary conditions. The solutions are presented in terms of the dimensionless variables given in (11), and unless otherwise stated the material properties used are given in Table 1.

Aside from the patch test, we will consider a linear elastic half-space $y \quad (0)$ subjected to either a time-dependent temperature change or heat flux on its boundary plane, free of traction. The following initial boundary value problems based on these conditions can be obtained: (a) the first Danilovskaya problem [18], (b) the second Danilovskaya problem [19], and (c) the Sternberg and Chakravorty problem [56]. These problems can be treated as one-dimensional, and can yield either coupled or uncoupled thermoelasticity.

9.1 Patch test for thermoelasticity

In this example, a one-dimensional patch test is performed to verify the exactness of the proposed VCI approach. The steady equations of energy and equilibrium on a domain $\Omega =]0, 1[$ can be cast as

$$\left(\frac{E}{1 \quad \nu^2}\right) \frac{\partial^2 u}{\partial x^2} \quad \beta \frac{\partial \theta}{\partial x} + b = 0 \quad \text{in } \Omega, \tag{81a}$$

$$k \frac{\partial^2 \theta}{\partial x^2} + Q = 0 \quad \text{in } \Omega. \tag{81b}$$

The boundary conditions considered here are

$$u(0) = 0, \quad u(1) = g, \tag{82a}$$

$$\theta(0) = 0, \quad \theta(1) = g. \tag{82b}$$

Linear solutions in both fields can be obtained using the following prescribed values:

$$b = \beta, \quad Q = 0, \quad g = 1, \tag{83}$$

which yields the exact solution of this problem for the two fields as

$$u = x, \quad \theta = x. \tag{84}$$

The discretized steady equations (81) yield the following matrix form:

$$\begin{bmatrix} \mathbf{K}_{uu} & \mathbf{K}_{u\theta} \\ \mathbf{0} & \mathbf{K}_{\theta\theta} \end{bmatrix} \begin{Bmatrix} \boldsymbol{u} \\ \theta \end{Bmatrix} = \begin{Bmatrix} \mathbf{F}^{\mathsf{ext}} \\ \mathbf{Q}^{\mathsf{ext}} \end{Bmatrix}. \tag{85}$$

It is important to note that for uniform discretizations, good accuracy or even exact solutions can be obtained by various integration methods, but in non-uniform discretizations, most methods fail the patch test. Therefore, the non-uniform discretization of the one dimensional domain shown in Figure 3 is employed in the study.

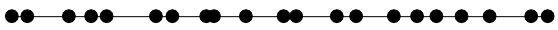

Figure 3: Non-uniform node distribution in one dimension

The dimensionless parameters $E = 1$, $\nu = 0.3$, and $\beta = 0.05$ are used in the patch test. As shown in Table 2, VC-DNI and the VC-NSNI pass the patch test (with machine precision) as expected. It can be seen that VC-DNI yields acceptable results for static thermoelasticity, but as will be seen in the next section, not for quasi-static and dynamic thermoelasticity. It is also notable that NSNI can drastically reduce the error without VC corrections. However, it will also be seen later that these treatments are still necessary to obtain good accuracy across all problems tested.

	DNI	VC-DNI	NSNI	VC-NSNI
u	0.2174	1.4418E-14	0.0035	1.6187E-13
θ	0.2113	1.2204E-14	0.0035	5.6947E-15

Table 2: L_2 norm of error for various methods in a 1-D static thermoelastic patch test

9.2 Quasi-static benchmarks: the first Danilovskaya problem

In this subsection, we study the quasi-static case of the first Danilovskaya problem under various discretizations and quadrature schemes. The first Danilovskaya problem [18] concerns a linear elastic half-space subjected to a uniform sudden temperature change on its boundary, with free traction. The boundary conditions in this problem are given as

$$\theta(0,t) = \theta_0, \tag{86a}$$

$$\sigma(0,t) = 0. \tag{86b}$$

The quasi-static problem neglects inertial effects, and the semi-discretized equations are

$$\mathbf{C}\dot{\mathbf{d}}(t) + \mathbf{K}\mathbf{d}(t) = \mathbf{F}(t). \tag{87}$$

9.2.1 Stability study

First, the stability of the proposed methods is studied. Uniform discretizations are employed, where spatial stability is more problematic in nodal integration [49, 24].

The spatial distributions of temperature change and displacement at $\bar{t} = 2$ are presented in Figures 4 and 5, respectively. It can be seen that DNI provides wildly unstable results, as before, for both the coupled and uncoupled cases. The node-to-node oscillations are typical of instability in nodal integration, yet here it is again seen these are orders of magnitude higher than pure elasticity.

The VC test function correction of DNI fails to provide any additional stability to the solution. This can be explained easily. The source of the instability is the calculation of meshfree gradients of the trial functions, not the test functions [24]. Therefore, the stability of the solution will not be affected by the selection of the test function. In [27] it was shown that while VC corrections can provide additional stability in non-uniform discretizations, they fail to provide it in uniform discretizations. Therefore additional stability must be provided by other means for the solution to be stable across all types of discretizations. Taking another point of view, in uniform discretizations the residuals of the integration constraints are generally very low [14, 11, 66]. Meanwhile, the VC corrections are driven by the residual, so little to no modification to the overall numerical method is made in this case.

Finally, both NSNI and VC-NSNI provide both stable and accurate results, with solutions comparable to the more expensive high-order Gaussian quadrature. Here the analytical solution is available for both the coupled and uncoupled cases.

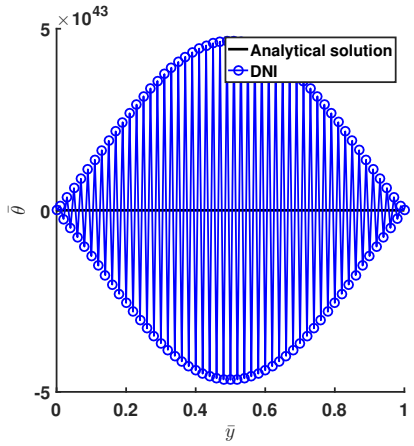

(a) DNI: $\delta = 1$

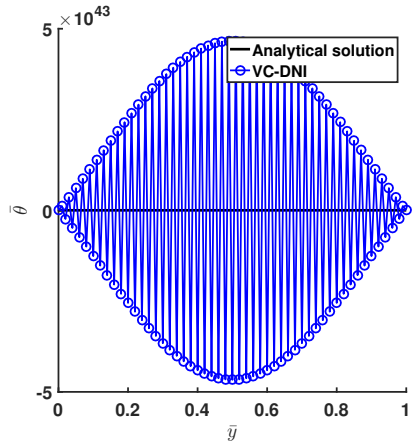

(b) VC-DNI: $\delta = 1$

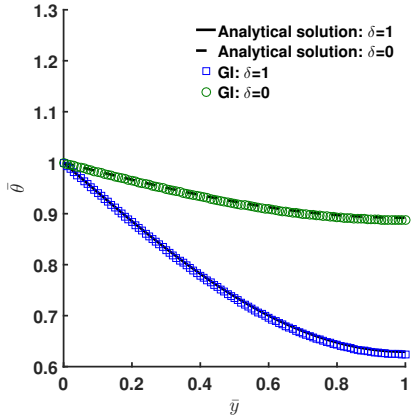

(c) GI

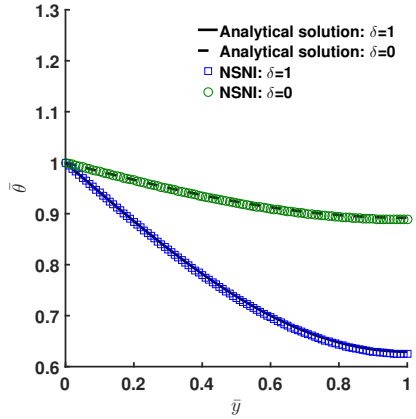

(d) NSNI

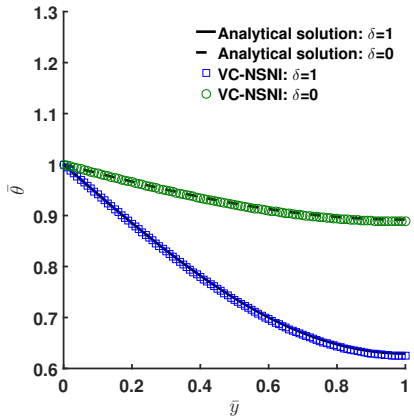

(e) VC-NSNI

Figure 4: Temperature changes along $\bar{y}$ at $\bar{t} = 2$ for the first Danilovskaya problem in a quasi-static uniform discretization with various methods.

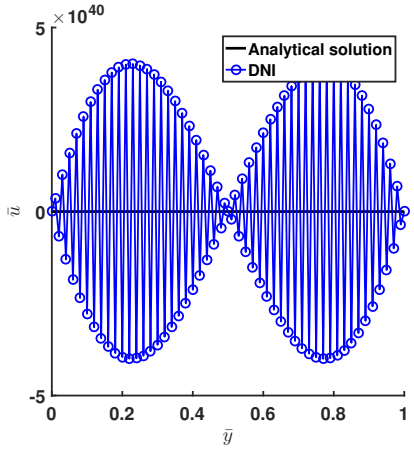

(a) DNI: $\delta = 1$

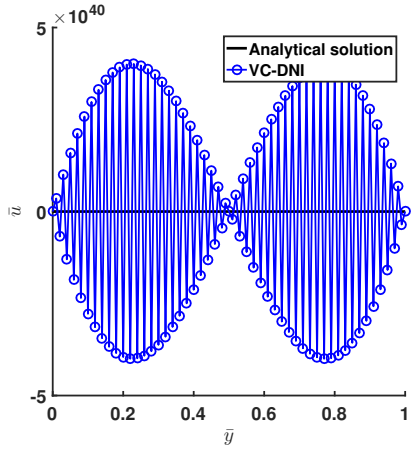

(b) VC-DNI: $\delta = 1$

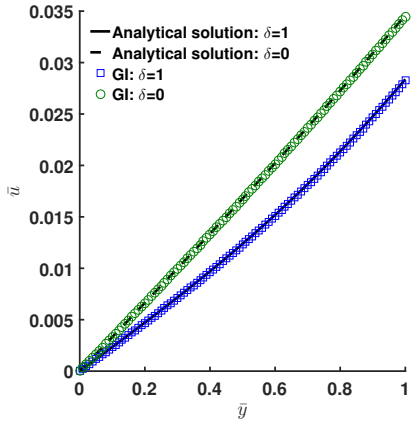

(c) GI

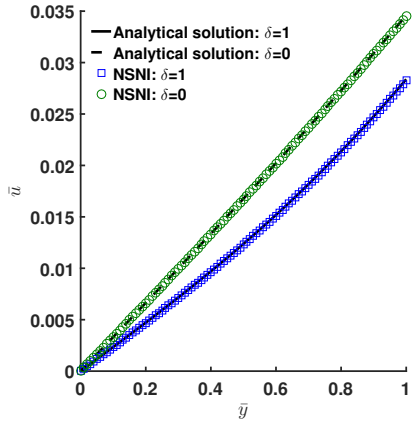

(d) NSNI

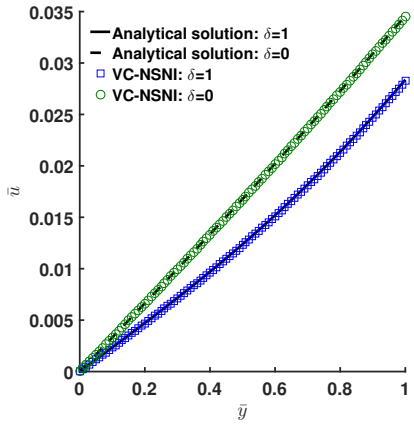

(e) VC-NSNI

Figure 5: Displacements along $\bar{y}$ at $\bar{t} = 2$ for the first Danilovskaya problem in a quasi-static uniform discretization with various methods.

Figures 6 and 7 show the time histories of temperature change and displacement at $\bar{y} = 1$, respectively, where explosive growth over time is seen in DNI for both fields, in both the coupled and uncoupled cases. Also seen in the figures, NSNI provides stable solutions, in both pure NSNI, and VC-NSNI. The VC correction here also does not provide much, which is expected as previously discussed.

As we have seen, Gauss integration was considered in this study. Here stable and accurate results were obtained, yet this method needs at least five-point quadrature to converge [11], which in turn is computationally demanding. On the other hand, the proposed RKPM formulation using VC-NSNI can provide comparable accuracy and stability with just one-point integration.

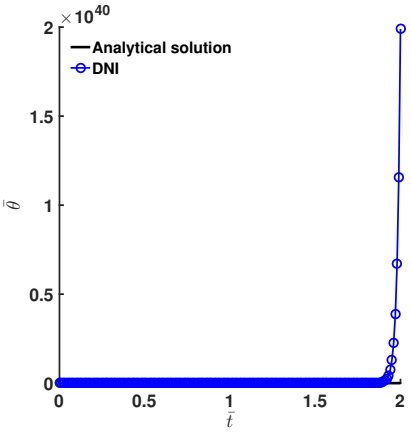

(a) DNI: $\delta = 1$

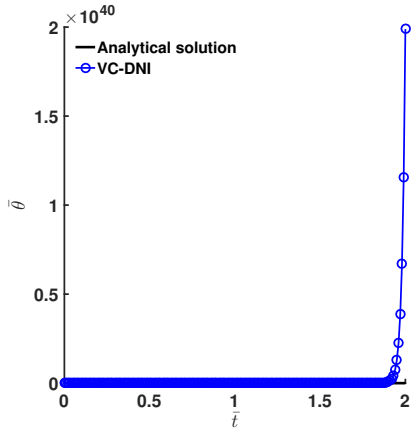

(b) VC-DNI: $\delta = 1$

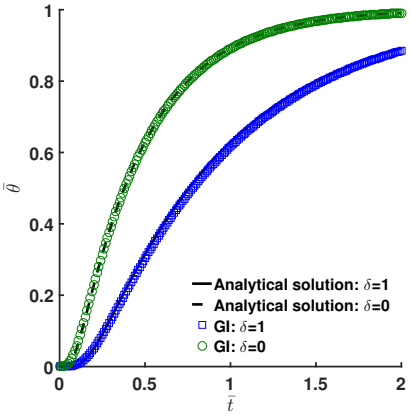

(c) GI

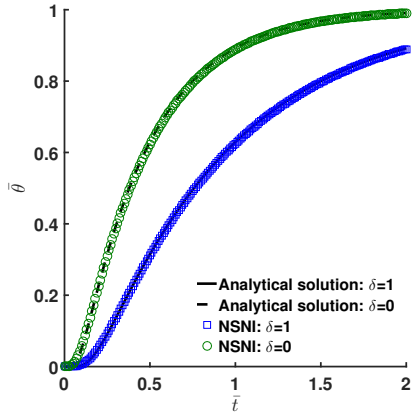

(d) NSNI

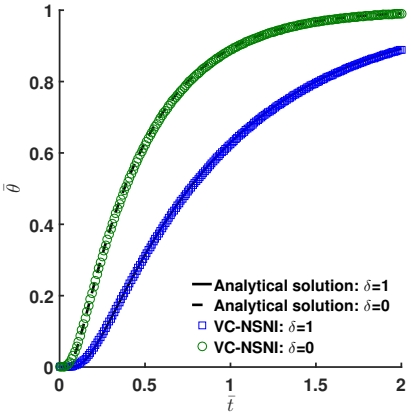

(e) VC-NSNI

Figure 6: Time histories of temperature change at $\bar{y} = 1$ for the first Danilovskaya problem in a quasi-static uniform discretization with various methods.

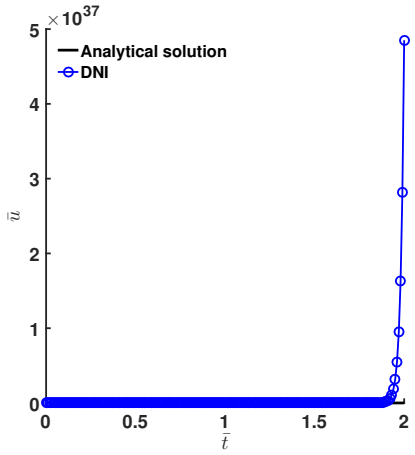

(a) DNI: $\delta = 1$

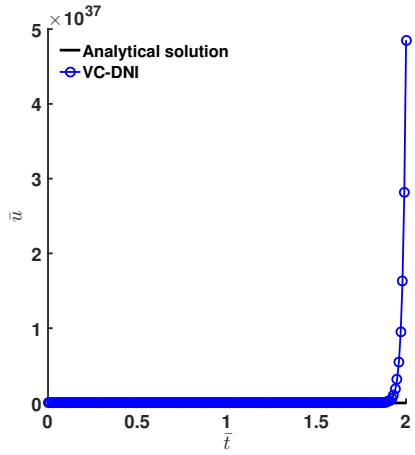

(b) VC-DNI: $\delta = 1$

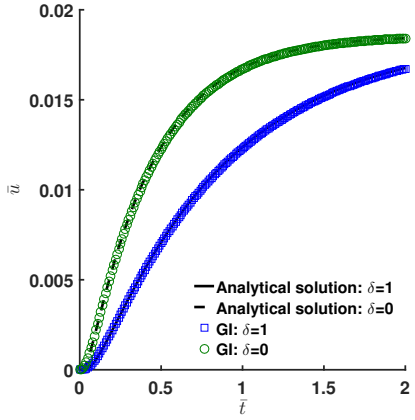

(c) GI

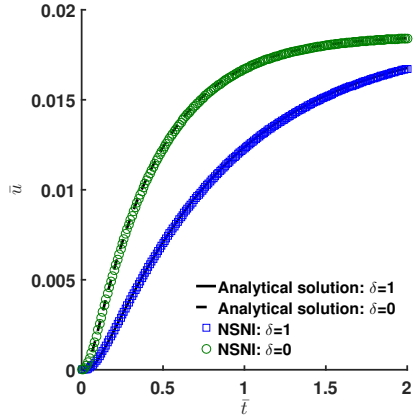

(d) NSNI

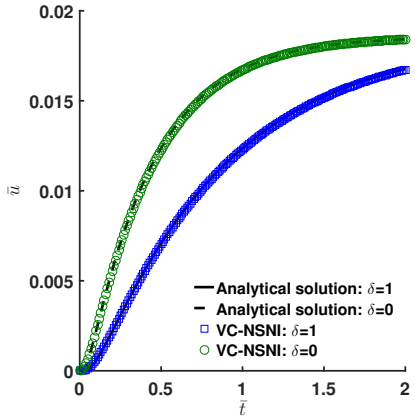

(e) VC-NSNI

Figure 7: Time histories of displacement at $\bar{y} = 1$ for the first Danilovskaya problem in a quasi-static uniform discretization with various methods.

9.2.2 Accuracy study

A non-uniform discretization is now considered to demonstrate the accuracy of the present approach. Largely, uniform discretizations are special cases where high accuracy can be obtained in meshfree methods regardless of the quadrature technique (excluding pure nodal integration which is unstable).

Here, since DNI provides completely unstable results, while Gauss integration is prohibitively expensive, only NSNI and VC techniques are considered.

Unlike in a uniform discretization, Figures 8 and 9 show that while pure NSNI can still provide stable results, it fails to provide good accuracy. There are large errors in the solution of NSNI, clearly observed in Figure 8a. The inaccuracy in the spatial distributions of the fields also manifest in the time histories shown in Figures 10 and 11. On the other hand, VC-NSNI provides both stability and high accuracy in the solution, in both spatial distributions and time histories. Thus, nodally integrated RKPM using VC-NSNI is the best candidate for integration in thermoelasticity considering all the methods tested, and VC-NSNI will be generally employed for the remainder of the examples.

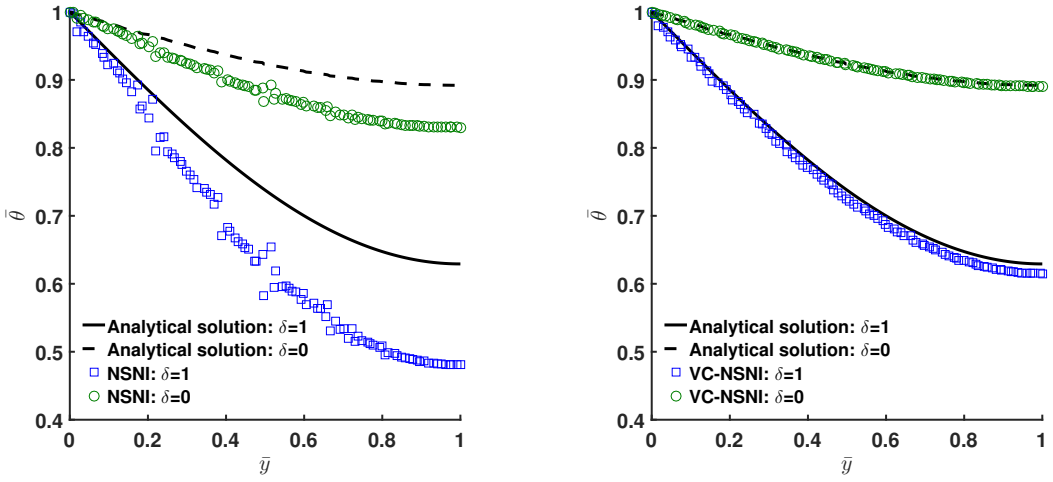

(a) NSNI (b) VC-NSNI

Figure 8: Temperature change along $\bar{y}$ at $\bar{t} = 2$ for the first Danilovskaya problem in a quasi-static nonuniform discretization and various methods.

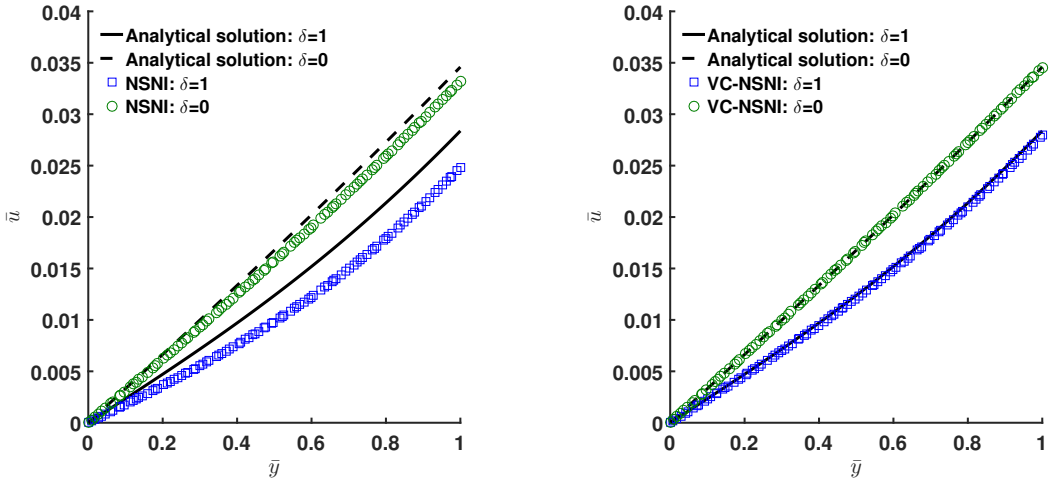

(a) NSNI (b) VC-NSNI

Figure 9: Displacement along $\bar{y}$ at $\bar{t} = 2$ for the first Danilovskaya problem in a quasi-static nonuniform discretization and various methods.

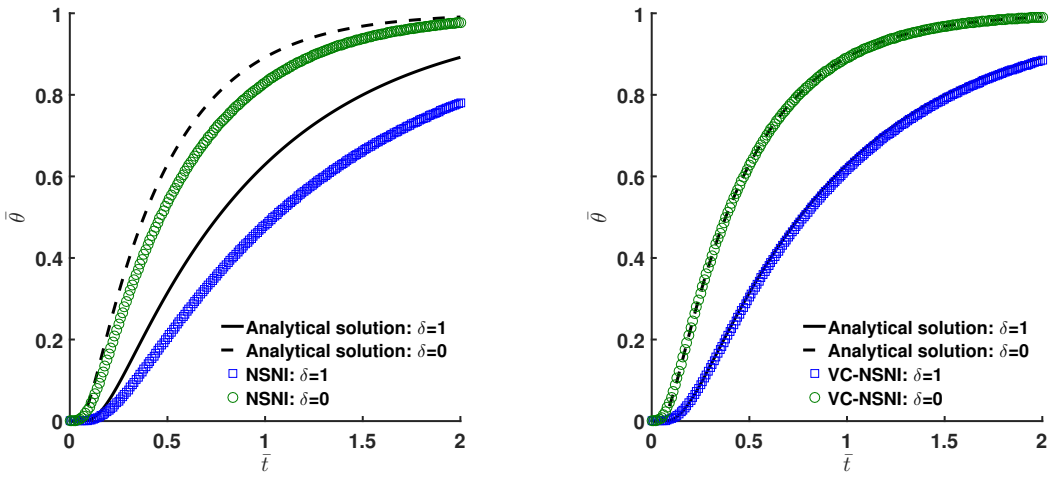

(a) NSNI (b) VC-NSNI

Figure 10: Time histories of temperature change at $\bar{y} = 1$ for the first Danilovskaya problem in a quasi-static nonuniform discretization and various methods.

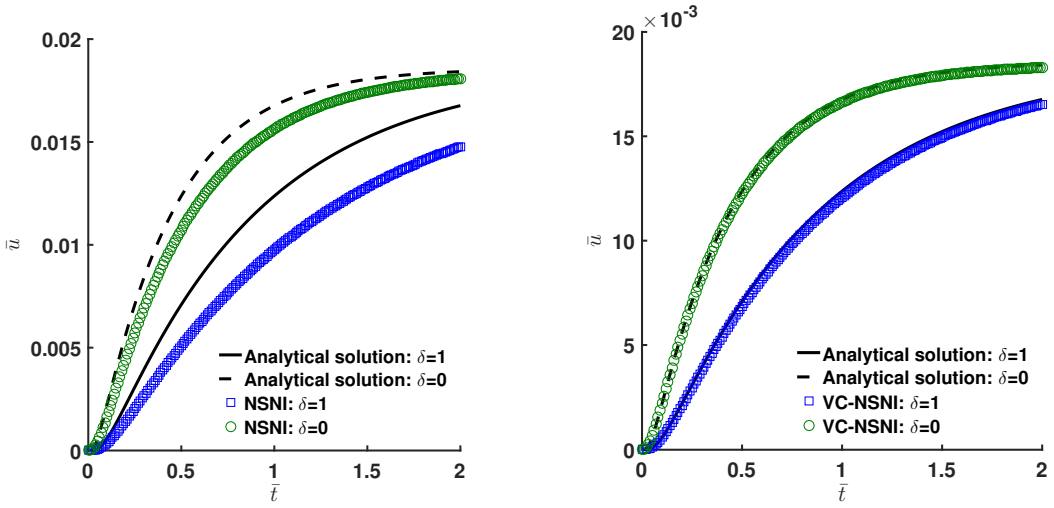

(a) NSNI (b) VC-NSNI

Figure 11: Time histories of displacement at $\bar{y} = 1$ for the first Danilovskaya problem in a quasi-static nonuniform discretization and various methods.

9.2.3 Convergence study

To study the convergence of the solution under refinement of the nodal spacing Δx, NSNI under a uniform nodal distribution is selected since it provides both stable and accurate results in this setting. Four NSNI discretizations of $\Delta x = 0.1, 0.05, 0.025$, and 0.01 are selected, and the results are shown in Figure 12. Clearly, the error for both fields converge, in both the coupled and uncoupled cases.

It can be seen that the displacements for both the coupled and uncoupled cases are not affected much by the nodal spacing Δx, since high accuracy is already obtained under course discretizations. For temperature change, both coupled and uncoupled cases are much more sensitive to Δx. Thus if temperature is of interest, it appears one must take care in the level of refinement necessary to obtain an acceptable solution. Here we remark that while $\Delta x = 0.01$ provides fairly acceptable results, the previous results using $\Delta x = 0.001$ obtained very high accuracy in VC-NSNI.

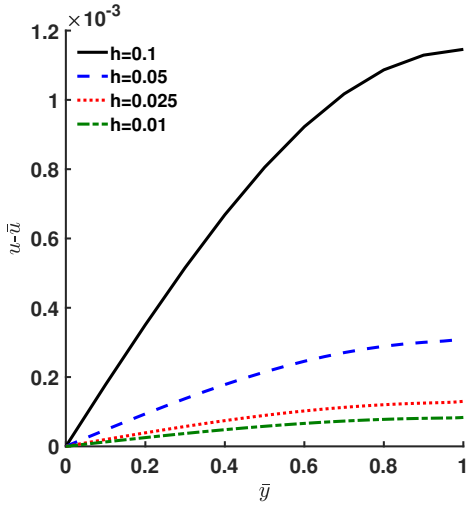

(a) Error of displacement: $\delta = 0$

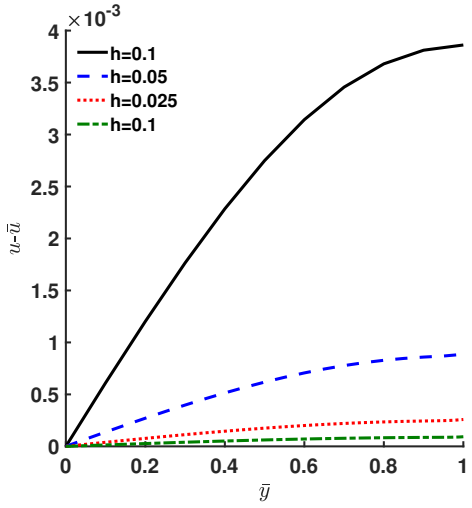

(b) Error of displacement: $\delta = 1$

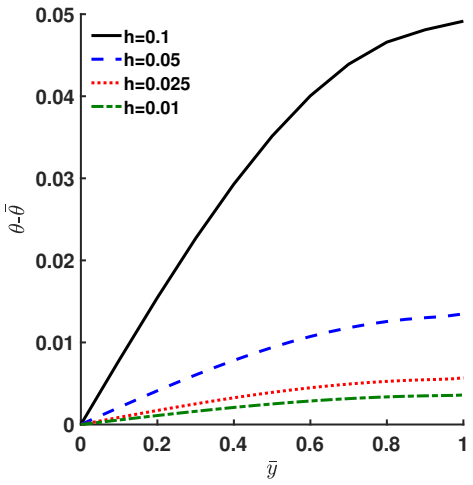

(c) Error of temperature change: $\delta = 0$

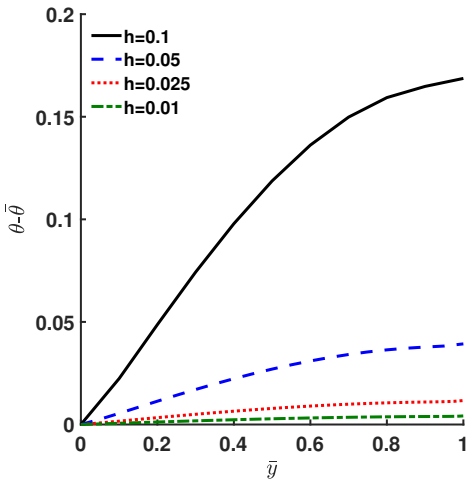

(d) Error of temperature change: $\delta = 1$

Figure 12: Convergence study along $\bar{y}$ at $\bar{t} = 2$ for the first Danilovskaya problem in a quasi-static uniform discretization with NSNI.

9.3 Dynamic benchmarks

The next examples consider inertial dynamic terms, where the full equation (77) is used to study dynamic thermoelasticity. VC-NSNI is employed to test the accuracy and stability of the RKPM solution.

9.3.1 First Danilovskaya problem: dynamic case

The first Danilovskaya problem has analytical solutions for the dynamic uncoupled case ($\delta = 0$), but not the coupled case ($\delta = 1$). As such, results from the DMLPG method in [23], and FEM in [34] are used for verification of the present VC-NSNI solution.

The time histories at $\bar{y} = 1$ for the temperature change and displacement are shown in Figures 13 and 14, respectively. For the uncoupled case, the RKPM solution matches well with the analytical solution with almost no error. The dramatic shift in displacement at $\bar{t} = 1$ is well-captured, with no oscillations despite the weak discontinuity in time. For the coupled case, the present method agrees well with the reference numerical solutions from the literature. Moreover, RKPM can also capture the transition point well in this case, more so than the other numerical methods.

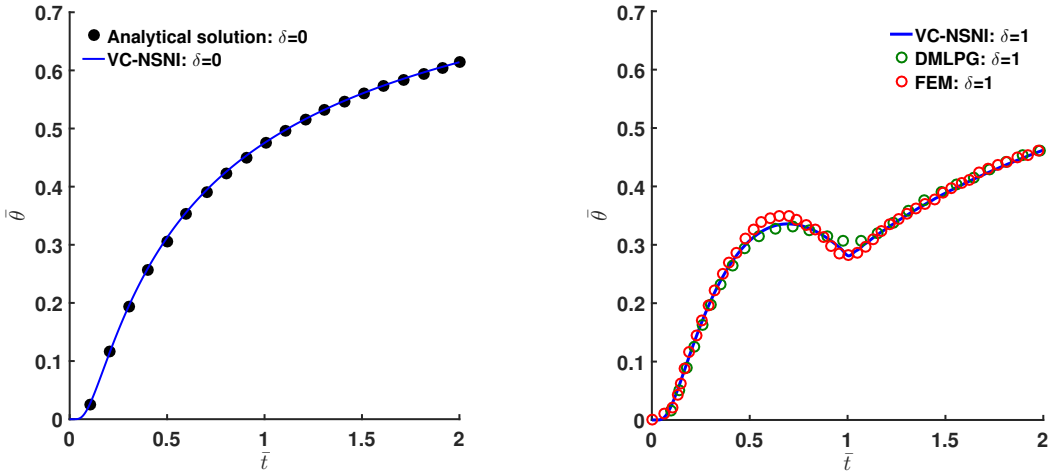

(a) Uncoupled case, $\delta = 0$.

(b) Coupled case, $\delta = 1$.

Figure 13: Temperature time history for the first Danilovskaya problem, dynamic.

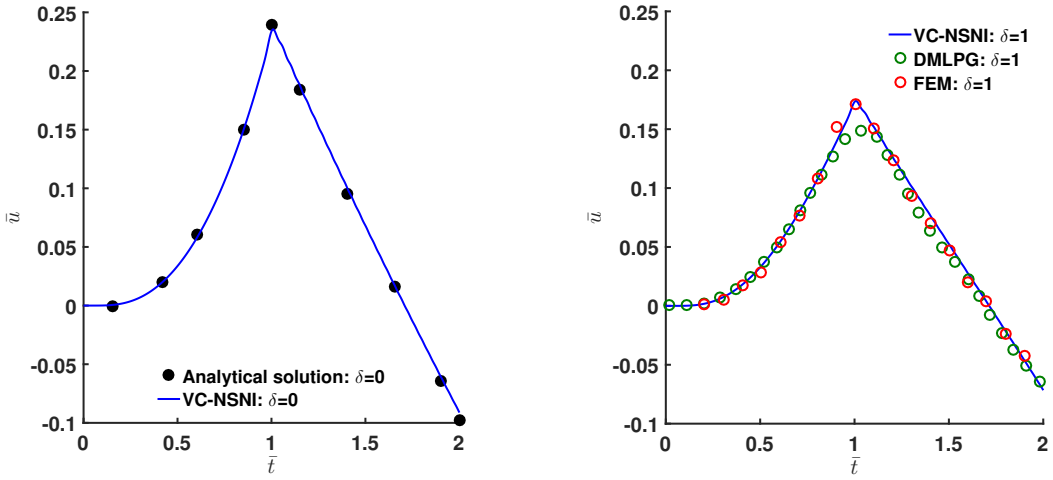

(a) Uncoupled case, $\delta = 0$.

(b) Coupled case, $\delta = 1$.

Figure 14: Displacement time history for the first Danilovskaya problem, dynamic.

Time histories for the stresses at $\bar{y} = 1$ for the coupled and uncoupled cases are shown in Figure 15. To explain the discontinuous response: the suddenly applied temperature can be modeled as a complementary error function, so the propagation of the stress wave is discontinuous. The derivation of the stress wave front and jump discontinuity can be found in [58]. For the uncoupled case, it can be seen that the solution matches well with the analytical solution, with no observable oscillation. For the coupled case this is also true, yet here the other numerical methods do oscillate in time across the discontinuity, and MLPG also smears the wave front.

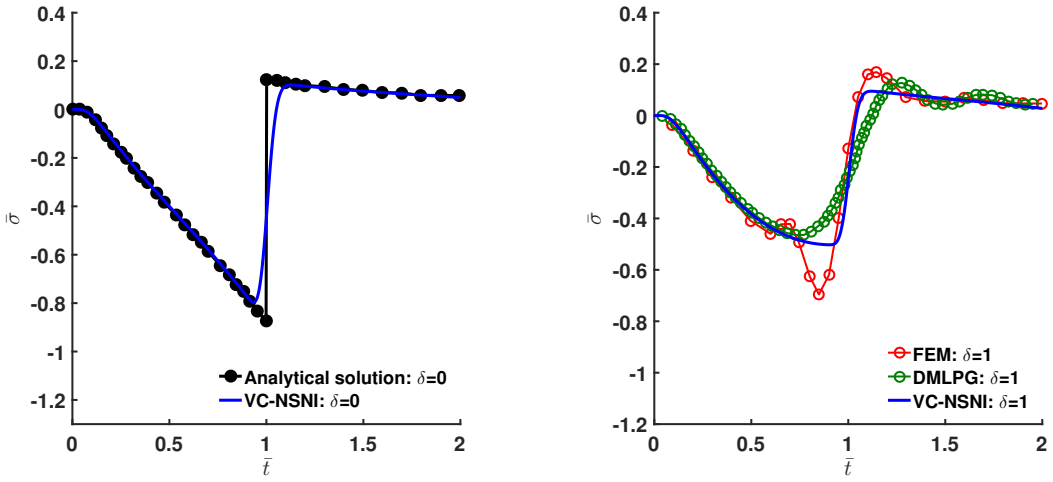

(a) Uncoupled case, $\delta = 0$.

(b) Coupled case, $\delta = 1$.

Figure 15: Stress time history for the first Danilovskaya problem, dynamic.

9.3.2 The second Danilovskaya problem

Next we consider a heat flux condition on the boundary $\bar{y} = 0$, which is the second Danilovskaya problem [19], an extended version of the first Danilovskaya problem. The boundary conditions are

$$\begin{cases} \sigma(0,t) = 0 \\ kT_{,y} = b(T \quad T_1) \end{cases} \tag{88}$$

where b is the boundary-layer conductance and T_1 the ambient temperature. Based on [59], these conditions can be expressed as:

$$q(y,\bar{t}) = m(1 \quad \theta(\bar{y},\bar{t})) \quad \text{on} \quad \bar{y} = 0 \tag{89}$$

where

$$m = \frac{\rho\kappa b}{(\lambda + 2\mu)k}. \tag{90}$$

A parameter of $m = 0.5$ is used in this study to select the free variable b. The temperature difference and displacement at $\bar{y} = 1$ are shown in Figure 16. Both of the coupled and uncoupled results obtained by VC-NSNI are in agreement with analytical solutions. Although the results of temperature change are slightly smaller than analytical solutions after $\bar{t} = 1.5$, they still seem acceptable since they match the general trend.

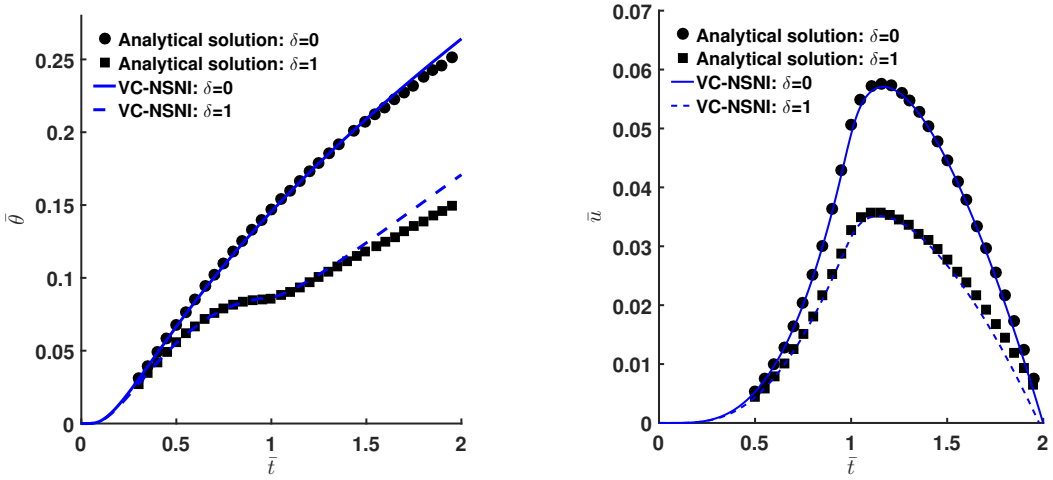

(a) Temperature change

(b) Displacement

Figure 16: Time histories for the second Danilovskaya problem.

9.3.3 The Sternberg and Chakravorty problem

The third benchmark considered uses a ramp-type heating, a more realistic boundary condition, on the boundary $\bar{y} = 0$, which is the Sternberg and Chakravorty problem [56]. The boundary conditions are

$$\tilde{\theta}(\bar{y},t) = \begin{cases} \tilde{\theta}/\theta & 0 \quad \tilde{\theta} \quad \theta \\ 1 & \tilde{\theta} \quad \theta \end{cases}. \tag{91}$$

We consider $\tilde{\theta} = 0.25$ and the coupled case with $\delta = 1$. Figure 17 shows the time histories of temperature change and displacement at $\bar{y} = 1$ obtained from the proposed nodally integrated RKPM technique, and analytical solution [46], where the results agree well. Similar to the previous benchmark, there are small differences between numerical and analytical results for the temperature difference after $\bar{t} = 1.5$, yet the RKPM results are still close, and the trend agrees well.

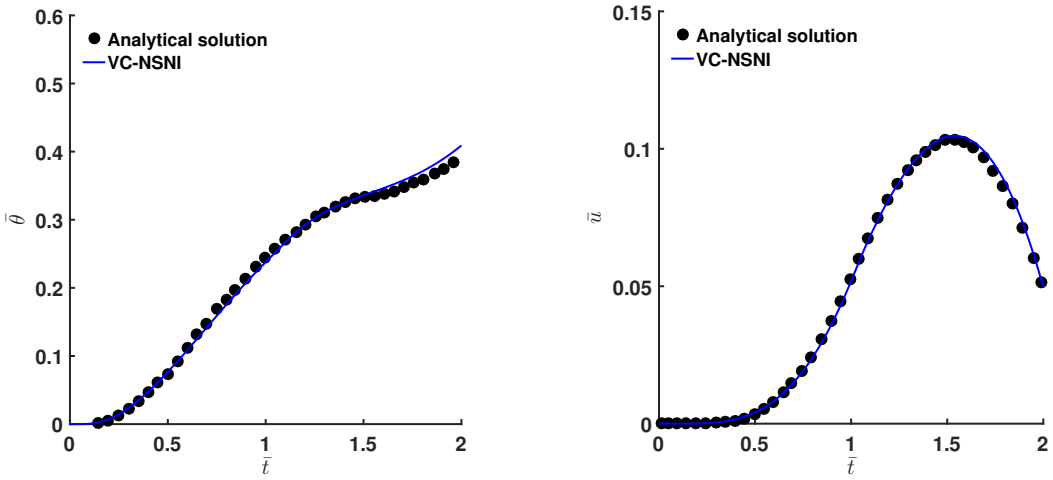

(a) Temperature change

(b) Displacement

Figure 17: Time histories for the Sternberg and Chakravorty problem in the coupled case, $\delta = 1$.

10 Conclusions

In part I of this paper, a stable, efficient, and accurate nodally integrated RKPM formulation has been developed for coupled and uncoupled thermoelasticity. It was first shown that nodal integration is highly unstable, yielding oscillations in the solution orders of magnitude higher than in pure elasticity. They grow seemingly unbounded and completely destroy the results. Thus it appears in this problem, stabilization of nodal integration is absolutely necessary.

To eliminate the spurious low energy modes that cause the oscillations, the NSNI scheme has been developed for the two-field problem. Analogous to the gradient expansion of the strain in solid mechanics, stabilization is introduced into the temperature gradient for a two-field NSNI.

To improve the poor accuracy induced by nodal integration, VCI is introduced by first deriving the variational consistency conditions for the two-field problem of thermoelasticity. Here it was found that there are three integration constraints due to the two governing equations and the coupling between them. This is in contrast to pure elasticity which has only one constraint. A uniform correction was then proposed for the test function gradients.

The patch test, first and second Danilovskaya problems, and the Sternberg and Chakravorty problem have been studied. The combined approach of VC-NSNI yields a stable, accurate and efficient RKPM solution to the coupled and uncoupled static, quasi-static, and dynamic benchmark problems. This was systematically shown through comparisons of RKPM results with analytical solutions, and solutions using other existing numerical methods.

In the sequel, these methods will be extended to generalized thermoelasticity, which provides a finite speed for the propagation of temperature, and thus a much less restrictive critical time step in explicit calculations. In addition, these techniques are developed for hyperbolic thermoplasticity, which also provides amenable conditions for explicit dynamics.

Acknowledgments The authors greatly acknowledge the support of this work by Penn State, and the endowment of the L. Robert and Mary L. Kimball Early Career Professorship. Proofing of this manuscript by Jennifer Dougal is also acknowledged and appreciated.

References

[1] J. Baek, J.-S. Chen, G. Zhou, K. Arnett, M. Hillman, G. Hegemier, and S. Hardesty. A semi-lagrangian reproducing kernel particle method with particle-based shock algorithm for explosive

welding simulation. *Computational Mechanics*, 67:1601–1627, 2021.

[2] S. Beissel and T. Belytschko. Nodal integration of the element-free Galerkin method. *Computer Methods in Applied Mechanics and Engineering*, 139:49–74, 1996.

[3] T. Belytschko, Y. Guo, W. K. Liu, and S. P. Xiao. A unifieded stability analysis of meshless particle methods. *International Journal for Numerical Methods in Engineering*, 48(9):1359–1400, 2000.

[4] F. Bobaru and S. Mukherjee. Meshless approach to shape optimization of linear thermoelastic solids. *International Journal for Numerical Methods in Engineering*, 53(4):765–796, 2002.

[5] B. A. Boley and I. S. Tolins. Transient coupled thermoelastic boundary value problems in the half-space. *Journal of Applied Mechanics*, 29(4):637–646, 1962.

[6] A. A. Cannarozzi and F. Ubertini. A mixed variational method for linear coupled thermoelastic analysis. *International Journal of Solids and Structures*, 38(4):717–739, 2001.

[7] J. P. Carter and J. R. Booker. Finite element analysis of coupled thermoelasticity. *Computers and Structures*, 31(1):73–80, 1989.

[8] J. Chen and G. F. Dargush. Boundary element method for dynamic poroelastic and thermoelastic analyses. *International Journal of Solids and Structures*, 32(15):2257–2278, 1995.

[9] J. Chen, W. Hu, M. Puso, Y. Wu, and X. Zhang. Strain smoothing for stabilization and regularization of galerkin meshfree methods. In *Meshfree methods for partial di erential equations III*, pages 57–75. Springer, 2007.

[10] J.-S. Chen, M. Hillman, and S.-W. Chi. Meshfree methods: progress made after 20 years. *Journal of Engineering Mechanics*, 143(4):04017001, 2017.

[11] J.-S. Chen, M. Hillman, and M. Rüter. An arbitrary order variationally consistent integration for Galerkin meshfree methods. *International Journal for Numerical Methods in Engineering*, 95(5):387–418, 2013.

[12] J.-S. Chen, C. Pan, C.-T. Wu, and W. K. Liu. Reproducing Kernel Particle Methods for large deformation analysis of non-linear structures. *Computer Methods in Applied Mechanics and Engineering*, 139(1-4):195–227, 1996.

[13] J.-S. Chen and H.-P. Wang. New boundary condition treatments in meshfree computation of contact problems. *Computer Methods in Applied Mechanics and Engineering*, 187(3-4):441–468, 2000.

[14] J.-S. Chen, C.-T. Wu, S. Yoon, and Y. You. A stabilized conforming nodal integration for galerkin mesh-free methods. *International journal for numerical methods in engineering*, 50(2):435–466, 2001.

[15] J.-S. Chen, S. Yoon, and C.-T. Wu. Non-linear version of stabilized conforming nodal integration for Galerkin mesh-free methods. *International Journal for Numerical Methods in Engineering*, 53(12):2587–2615, 2002.

[16] J.-S. Chen, X. Zhang, and T. Belytschko. An implicit gradient model by a reproducing kernel strain regularization in strain localization problems. *Computer Methods in Applied Mechanics and Engineering*, 193(27-29):2827–2844, 2004.

[17] H. K. Ching and S. C. Yen. Transient thermoelastic deformations of 2-D functionally graded beams under nonuniformly convective heat supply. *Composite Structures*, 73(4):381–393, 2006.

[18] V. Danilouskaya. Thermal stresses in elastic half space due to sudden heating of its boundary. *Pelageya Yakovlevna Kochina*, 14:316–321, 1950.

[19] V. Danilouskaya. On a dynamic problem of thermoelasticity. *Prikladnaya Matematika i Mekhanika*, 16:341–344, 1952.

[20] J. Dolbow and T. Belytschko. Numerical integration of the galerkin weak form in meshfree methods. *Computational mechanics*, 23(3):219–230, 1999.

[21] Q. Duan, X. Li, H. Zhang, and T. Belytschko. Second-order accurate derivatives and integration schemes for meshfree methods. *International Journal for Numerical Methods in Engineering*, 92(4):399–424, 2012.

[22] T.-P. Fries and T. Belytschko. Convergence and stabilization of stress-point integration in mesh-free and particle methods. *International Journal for Numerical Methods in Engineering*, 74(7):1067–1087, 2008.

[23] K. Hasanpour and D. Mirzaei. A fast meshfree technique for the coupled thermoelasticity problem. *Acta Mechanica*, 229(6):2657–2673, 2018.

[24] M. Hillman and J.-S. Chen. An accelerated, convergent, and stable nodal integration in Galerkin meshfree methods for linear and nonlinear mechanics. *International Journal for Numerical Methods in Engineering*, 107:603–630, 2016.

[25] M. Hillman and J.-S. Chen. Nodally integrated implicit gradient reproducing kernel particle method for convection dominated problems. *Computer Methods in Applied Mechanics and Engineering*, 299:381–400, 2016.

[26] M. Hillman and J.-S. Chen. Performance comparison of nodally integrated galerkin meshfree methods and nodally collocated strong form meshfree methods. In *Advances in Computational Plasticity*, pages 145–164. Springer, 2018.

[27] M. Hillman, J.-S. Chen, and S.-W. Chi. Stabilized and variationally consistent nodal integration for meshfree modeling of impact problems. *Computational Particle Mechanics*, 1(3):245–256, 2014.

[28] M. Hillman and K.-C. Lin. Consistent weak forms for meshfree methods: Full realization of h-refinement, p-refinement, and a-refinement in strong-type essential boundary condition enforcement. *Computer Methods in Applied Mechanics and Engineering*, 373:113448, 2021.

[29] P. Hosseini-Tehrani and M. R. Eslami. BEM analysis of thermal and mechanical shock in a two-dimensional finite domain considering coupled thermoelasticity. *Engineering Analysis with Boundary Elements*, 24(3):249–257, 2000.

[30] H.-Y. Hu, C.-K. Lai, and J.-S. Chen. A study on convergence and complexity of reproducing kernel collocation method. *Interaction and multiscale mechanics*, 2(3):295–319, 2009.

[31] T. J. Hughes. *The nite element method: linear static and dynamic nite element analysis*. Dover Publications, Inc., Mineola, New York, 2012.

[32] K. K. Tamma and S. B. Railkar. On heat displacement based hybrid transfinite element formulations for uncoupled/coupled thermally induced stress wave propagation. *Computers and Structures*, 30:1025–1036, 1988.

[33] G. A. Keramidas and E. C. Ting. A finite element formulation for thermal stress analysis. Part I: Variational formulation. *Nuclear Engineering and Design*, 39(2-3):267–275, 1976.

[34] G. A. Keramidas and E. C. Ting. A finite element formulation for thermal stress analysis. Part II: Finite element formulation. *Nuclear Engineering and Design*, 39(2-3):277–287, 1976.

[35] S. Li and W. K. Liu. Synchronized reproducing kernel interpolant via multiple wavelet expansion. *Computational Mechanics*, 21:28–47, 1998.

[36] S. Li and W. K. Liu. Reproducing kernel hierarchical partition of unity, part I - formulation and theory. *International Journal for Numerical Methods in Engineering*, 288(July 1998):251–288, 1999.

[37] S. Li and W. K. Liu. Reproducing kernel hierarchical partition of unity, Part II - applications. *International Journal for Numerical Methods in Engineering*, 45(3):289–317, 1999.

[38] G.-R. Liu, G. Y. Zhang, Y. Y. Wang, Z. H. Zhong, G. Y. Li, and X. Han. A nodal integration technique for meshfree radial point interpolation method (NI-RPIM). *International Journal of Solids and Structures*, 44(11-12):3840–3860, 2007.

[39] W. K. Liu, S. Jun, and Y. F. Zhang. Reproducing kernel particle methods. *International Journal for Numerical Methods in Fluids*, 20(8-9):1081–1106, 1995.

[40] W.-K. Liu, S. Li, and T. Belytschko. Moving least-square reproducing kernel methods (i) methodology and convergence. *Computer methods in applied mechanics and engineering*, 143(1-2):113–154, 1997.

[41] W. K. Liu, J. S.-J. Ong, and R. A. Uras. Finite element stabilization matrices — a unification approach. *Computer Methods in Applied Mechanics and Engineering*, 53(1):13–46, 1985.

[42] A. Mahdavi, S.-W. Chi, and M. M. Atif. A two-field semi-lagrangian reproducing kernel model for impact and penetration simulation into geo-materials. *Computational Particle Mechanics*, 7(2):351–364, 2020.

[43] A. Mahdavi, S.-W. Chi, and H. Zhu. A gradient reproducing kernel collocation method for high order differential equations. *Computational Mechanics*, 64(5):1421–1454, 2019.

[44] G. Moutsanidis, W. Li, and Y. Bazilevs. Reduced quadrature for FEM, IGA and meshfree methods. *Computer Methods in Applied Mechanics and Engineering*, 373:113521, 2021.

[45] T. Nagashima. Node-by-node meshless approach and its applications to structural analyses. *International Journal for Numerical Methods in Engineering*, 46(3):341–385, 1999.

[46] J. L. Nickell, Robert E and Sackman. Approximate solutions in linear, coupled thermoelasticity. *Journal of Applied Mechanics*, 35(2):255–266, 1968.

[47] W. Nowacki. *Dynamic problems of thermoelasticity*. Springer Science & Business Media, 1975.

[48] J.-H. Prevost and D. Tao. Finite element analysis of dynamic coupled thermoelasticity problems with relaxation times. *Journal of applied mechanics*, 50(4a):817–822, 1983.

[49] M. A. Puso, J.-S. Chen, E. Zywicz, and W. Elmer. Meshfree and finite element nodal integration methods. *International Journal for Numerical Methods in Engineering*, 74(3):416–446, 2008.

[50] L. F. Qian and R. C. Batra. Transient Thermoelastic Deformations of a thick functionally graded plate. *Journal of Thermal Stresses*, 27(8):705–740, 2004.

[51] P. W. Randles and L. D. Libersky. Normalized SPH with stress points. *Int. J. Numer. Meth. Engng*, 48(May 1999):1445–1462, 2000.

[52] M. Rüter, M. Hillman, and J.-S. Chen. Corrected stabilized non-conforming nodal integration in meshfree methods. In *Meshfree methods for partial di erential equations VI*, pages 75–92. Springer, 2013.

[53] T. Siriaksorn, S.-W. Chi, C. Foster, and A. Mahdavi. u-p semi-lagrangian reproducing kernel formulation for landslide modeling. *International Journal for Numerical and Analytical Methods in Geomechanics*, 42(2):231–255, 2018.

[54] J. Sladek, V. Sladek, P. Solek, C. L. Tan, and C. Zhang. Two- and three-dimensional transient thermoelastic analysis by the MLPG method. *Computer Modeling in Engineering and Sciences*, 47, 2009.

[55] V. Sládek and J. Sládek. Boundary element method in micropolar thermoelasticity. Part II: Boundary integro-differential equations. *Engineering Analysis*, 2(2):81–91, 1985.

[56] E. L. I. Sternberg and J. G. Chakravorty. *On inertia e ects in a transient thermoelastic problem.* Brown University, 1958.

[57] M. Tanaka, T. Matsumoto, and M. Moradi. Application of boundary element method to 3-D problems of coupled thermoelasticity. *Engineering Analysis with Boundary Elements*, 16(4):297–303, 1995.

[58] E. A. Thornton. *Thermal structures for aerospace applications*. American Institute of Aeronautics and Astronautics, 1996.

[59] N. Tosaka and I. G. Suh. Boundary element analysis of dynamic coupled thermoelasticity problems. *Computational Mechanics*, 8(5):331–342, 1991.

[60] D. Wang and J. Wu. An inherently consistent reproducing kernel gradient smoothing framework toward efficient Galerkin meshfree formulation with explicit quadrature. *Computer Methods in Applied Mechanics and Engineering*, 349:628–672, 2019.

[61] H. Wei, J.-S. Chen, F. Beckwith, and J. Baek. A naturally stabilized semi-lagrangian meshfree formulation for multiphase porous media with application to landslide modeling. *Journal of Engineering Mechanics*, 146(4):04020012, 2020.

[62] H. Wei, J.-S. Chen, and M. Hillman. A stabilized nodally integrated meshfree formulation for fully coupled hydro-mechanical analysis of fluid-saturated porous media. *Computers & Fluids*, 141:105–115, 2016.

[63] C.-T. Wu, S.-W. Chi, M. Koishi, and Y. Wu. Strain gradient stabilization with dual stress points for the meshfree nodal integration method in inelastic analyses. *International Journal for Numerical Methods in Engineering*, 107(1):3–30, 2016.

[64] C.-T. Wu, M. Koishi, and W. Hu. A displacement smoothing induced strain gradient stabilization for the meshfree Galerkin nodal integration method. *Computational Mechanics*, 2015.

[65] C. T. Wu, Y. Wu, D. Lyu, X. Pan, and W. Hu. The momentum-consistent smoothed particle Galerkin (MC-SPG) method for simulating the extreme thread forming in the flow drill screwdriving process. *Computational Particle Mechanics*, 7(2):177–191, 2020.

[66] J. Wu and D. Wang. An accuracy analysis of Galerkin meshfree methods accounting for numerical integration. *Computer Methods in Applied Mechanics and Engineering*, 375:113631, 2021.

[67] B. J. Zheng, X. W. Gao, K. Yang, and C. Z. Zhang. A novel meshless local Petrov-Galerkin method for dynamic coupled thermoelasticity analysis under thermal and mechanical shock loading. *Engineering Analysis with Boundary Elements*, 60:154–161, 2015.